Framework for idealized climate simulations with spatiotemporal stochastic clouds and planetary-scale circulations

Tianhong Huang, Samuel N. Stechmann, and Jason L. Torchinsky

Phys. Rev. Fluids **7**, 010502 — Published 20 January 2022

DOI: 10.1103/PhysRevFluids.7.010502

A framework for idealized climate simulations with spatiotemporal stochastic clouds and planetary-scale circulations

Tianhong Huang,* Samuel N. Stechmann, and Jason L. Torchinsky
University of Wisconsin–Madison
Madison, Wisconsin 53706

(Dated: Submitted August 4, 2021; Revised October 22, 2021; and December 13, 2021)

In climate predictions, clouds are the leading source of uncertainty. This is partly because, to simulate the fluid dynamics of climate over the entire globe, a large grid spacing must be used, so clouds are a subgrid-scale parameterization rather than a resolved feature. Here, a framework is investigated with finer grid spacing of $O(1)$ or $O(10)$ km so that some clouds are not subgrid-scale; instead, clouds evolve on the numerical grid. This cloud evolution is achieved using stochastic modeling. Hence the framework is idealized in the sense that the full fluid dynamics of cloud circulations is still not resolved, and simplified vertical structures are used. Nevertheless, the fluid dynamics model includes evolving clouds that interactively adjust in size, shape, lifetime, and regional coverage. In addition, different cloud types are included with different roles in the climate system, including deep convective clouds and also boundary-layer clouds such as shallow cumulus and stratocumulus clouds. Other basic aspects of the idealized climate system are planetary-scale circulations (e.g., Walker circulation) and radiation. With these ingredients (evolving clouds, planetary-scale circulations, and radiation), the framework has the potential for idealized investigations of climate change with interactive cloud–radiative feedback of individual clouds. Here, the formulation of the model equations is presented, and numerical simulations are shown to illustrate the model dynamics and climate change.

* thuang76@wisc.edu

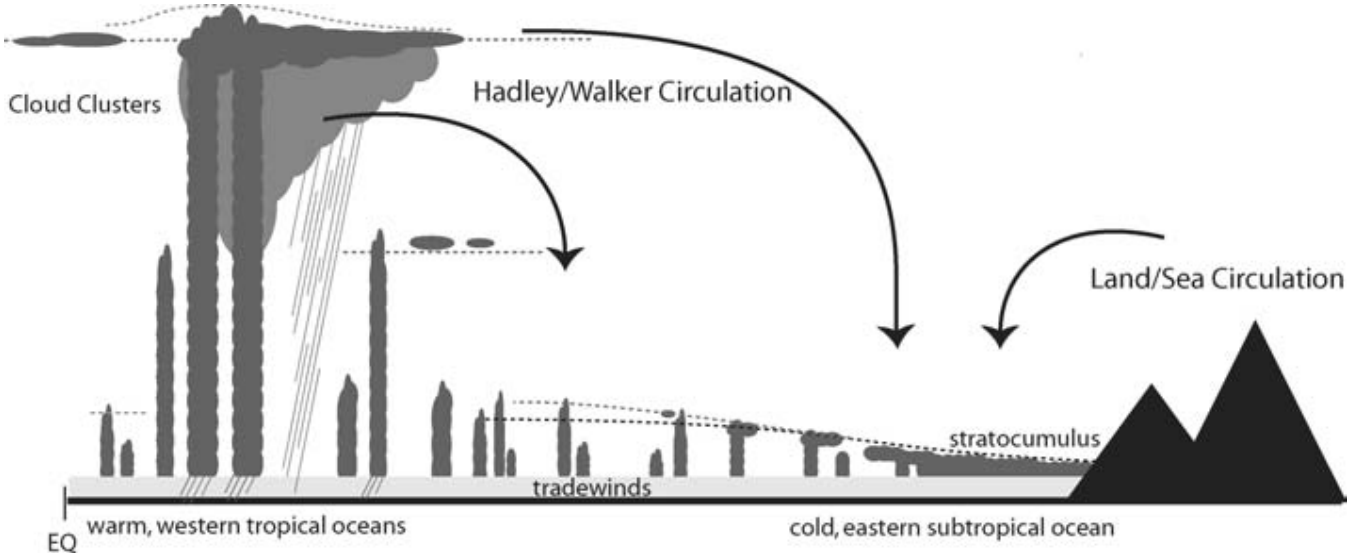

FIG. 1. Schematic diagram of cloud regimes and associated large-scale circulations. Deep convective clouds are associated with the ascending branch of the Walker circulation, and shallow clouds are associated with the descending branch of the Walker circulation. From Ref. 8. Used with permission.

I. INTRODUCTION

Global climate is influenced by both radiation and fluid dynamics. In the simplest models of climate, radiative transfer alone can be used to illustrate basic principles, such as the greenhouse effect due to carbon dioxide [1]. However, for more precise predictions of climate, the combined effects of radiation and atmospheric/oceanic fluid dynamics are needed, as in, for instance, contemporary global climate models (GCMs) [2, 3].

In GCM predictions of future climate change, the leading source of uncertainty is clouds [4–7]. Clouds can potentially have either a cooling effect or a warming effect. By reflecting solar radiation, clouds can have a cooling effect. On the other hand, clouds can absorb the radiation that is emitted by the earth's surface, and, in so doing, can produce a greenhouse warming effect in much the same way as carbon dioxide. Furthermore, different types of clouds (see Fig. 1) can have different effects on climate. For instance, shallow clouds near the earth's surface tend to have a greater cooling effect than warming effect. On the other hand, the deep clouds of a thunderstorm have both cooling and warming effects, and the cooling and warming effects can cancel each other and result in a near-zero impact on the radiation budget.

Moreover, it is important to emphasize that the difficulty is not only the clouds themselves but also their interaction with large-scale atmospheric fluid dynamics [2–7]. As illustrated in Fig. 1, different cloud types are associated with different components of large-scale circulations. For instance, deep convective clouds are associated with the ascending branch of the Walker circulation, and shallow clouds are associated with the descending branch. Hence the two phenomena—clouds and circulation—are inextricably linked, and uncertainties related to clouds are also uncertainties related to cloud–circulation interactions.

To properly account for the effects of clouds on climate, one would like to perform numerical simulations of atmospheric fluid dynamics. However, a major challenge is that clouds and climate operate across a vast range of scales. In Fig. 1, the small-scale features include shallow cumulus and stratocumulus clouds, which require a grid spacing of $O(100)$ m or $O(10)$ m or smaller in large eddy simulations (LES) [9–12]. On the large scales, on the other hand, is the Walker circulation, which spans scales of $O(10^6)$ or $O(10^7)$ m [13, 14]. For such a vast range of scales, LES or cloud-resolving models (CRMs) are computationally expensive. On a more limited scale, CRMs have been used to explore clouds, precipitation, and climate change, although typically only over a limited area on regional scales and not including large-scale circulations [15–18]. If restricted to 2D, a CRM could go as far as to simulate a Walker circulation and deep convection [19], although to also resolve stratocumulus clouds would be computationally expensive. Typically, to include large-scale circulations such as the Walker circulation, GCMs can be used, although the grid spacing is typically $O(10^4)$ or $O(10^5)$ m, which is too large to resolve individual clouds, so clouds are parameterized as a subgrid-scale process [2, 3] or resolved on fine scales as part of a multi-scale modeling framework [20]. In summary, due to computational expense, it is difficult to simultaneously simulate the full range of important scales in Fig. 1, from large-scale circulations to the individual cloud features of shallow clouds such as stratocumulus clouds.

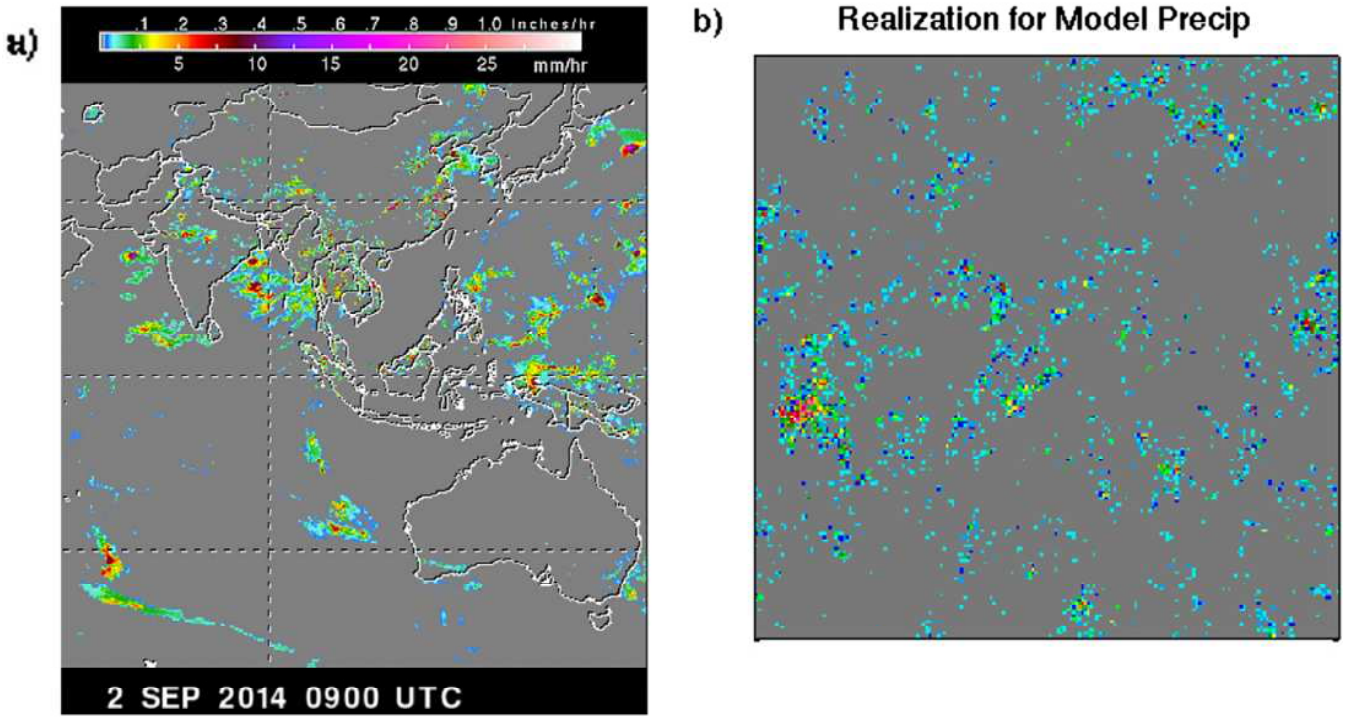

FIG. 2. Comparison of precipitation from (a) observational data and (b) stochastic model. Note that a stochastic model will not reproduce the exact same locations of individual cloud clusters in observational data on a particular day. The statistics, though, can be compared and are similar (in terms of, for instance, power spectral density and the pdf of cloud cluster area). From Ref. 21. © American Meteorological Society. Used with permission.

The goal of the present paper is to investigate another modeling framework, in addition to LES, CRMs, and GCMs, as a way of potentially simulating both large-scale circulations and shallow clouds such as stratocumulus clouds. The idea is to use a stochastic model for the spatiotemporal variability of clouds. Example snapshots from stochastic models are shown in Figs. 2 and 3 for deep convective and shallow clouds, respectively, to illustrate the level of statistical realism. Many cloud statistics can be simulated by stochastic models [21–25], including different regimes of shallow clouds such as stratocumulus clouds, which have been identified as the main contributor to cloud feedback uncertainties in GCM climate predictions [6]. Here, a stochastic model for shallow clouds [22] will be combined with a model for deep convection and large-scale atmospheric fluid dynamics [26–32], thereby encompassing the phenomena in Fig. 1, from shallow clouds on small scales to the Walker circulation on large scales.

A significant computational savings can be achieved by using stochastic models instead of LES. The computational savings comes in part from an increase in horizontal grid spacing, since LES of stratocumulus clouds would require a horizontal grid spacing of $O(10)$ or $O(100)$ m, whereas the stochastic models can use a horizontal grid spacing of $O(10^3)$ or $O(10^4)$ m. In addition, the vertical grid also provides a significant computational savings, since LES of stratocumulus clouds would require a vertical grid spacing of $O(10)$ or $O(100)$ m, whereas the stochastic models use simplified vertical structures, as illustrated in Fig. 4. The vertical structures in Fig. 4 arise from a Sturm–Liouville problem from the equations for atmospheric fluid dynamics [33, 34], and they are also the basic vertical structures associated with the deep convective clouds and Walker circulation in Fig. 1. As a result of the simplified vertical structure, the stochastic models have a computational grid with the number of dimensions reduced by one, from a three-dimensional (3D) grid to a two-dimensional (2D) grid.

With atmospheric fluid dynamics partially represented, the present framework is intermediate in complexity between, on the one hand, LES/CRM/GCM frameworks, and, on the other hand, simplified models such as two-box models that do not resolve detailed structures of atmospheric circulations (see Refs. 35 and 36 and references therein). While a two-box model can represent the widths of entire regions (such as one single grid box for the entire ascending branch of the Walker circulation and another grid box for the descending branch), the present framework can furthermore represent individual cloud clusters within those regions. It is also possible, within LES/CRM/GCM frameworks, to simulate both shallow clouds and large-scale circulations by using mesh refinement or grid stretching, which has been explored in a variety of different configurations [37–40], although at significant computational expense. While the present stochastic framework is idealized in comparison to LES/CRM/GCM frameworks, the stochastic framework

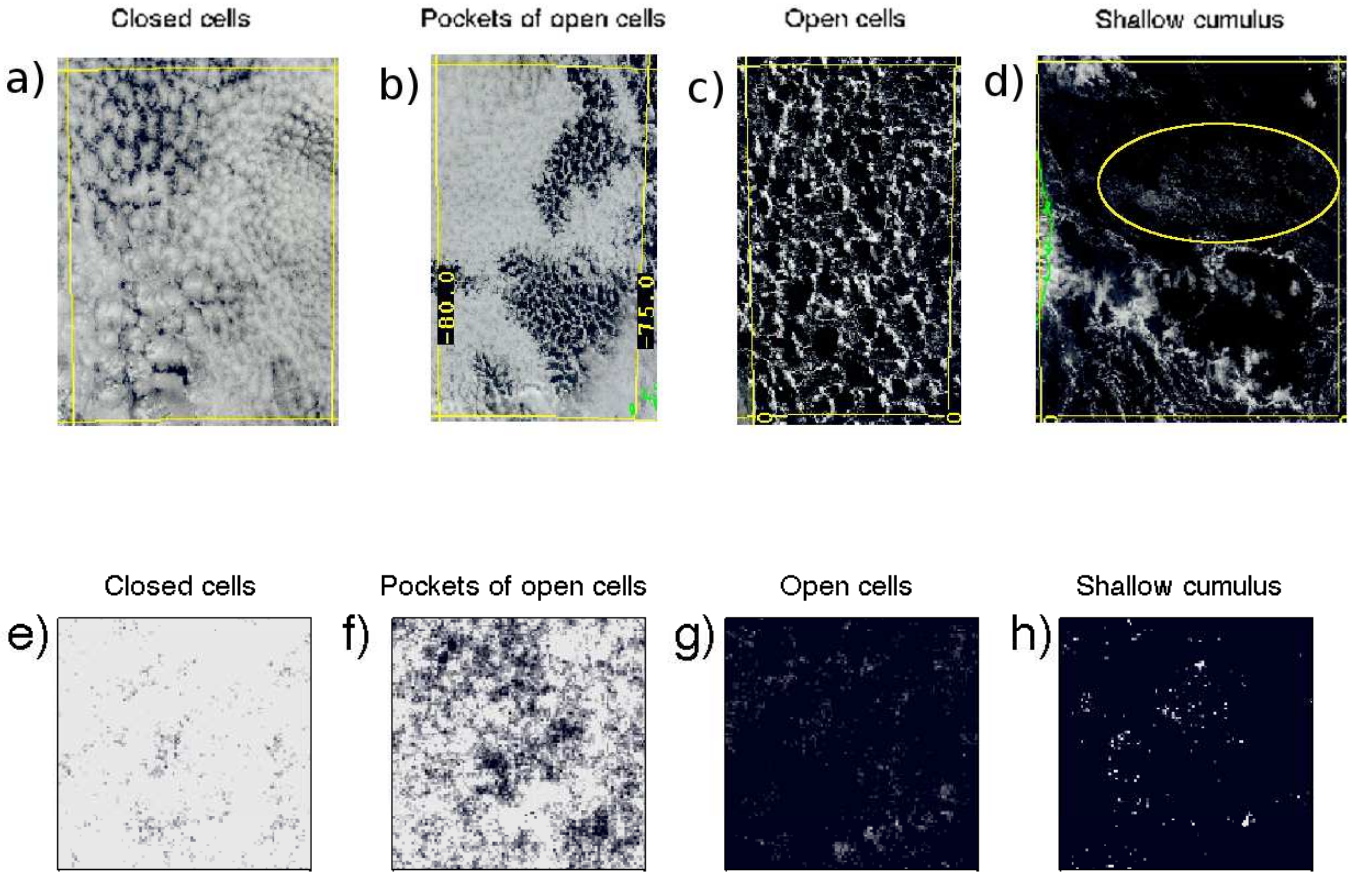

FIG. 3. Stochastic model representation [panels (e)–(h)] of four types of shallow cloud organization, as seen from satellite in panels (a)–(d). Yellow lines indicate areas of 5° longitude by 5° latitude. The model domain size is also 5° by 5°. From Ref. 22. Used with permission.

brings a large computational savings that can be invested in, for instance, faster exploration of parameter space and larger ensembles of simulations.

In the remainder of the paper, the model is described in section II, numerical simulations are presented in section III, and conclusions are summarized in section IV.

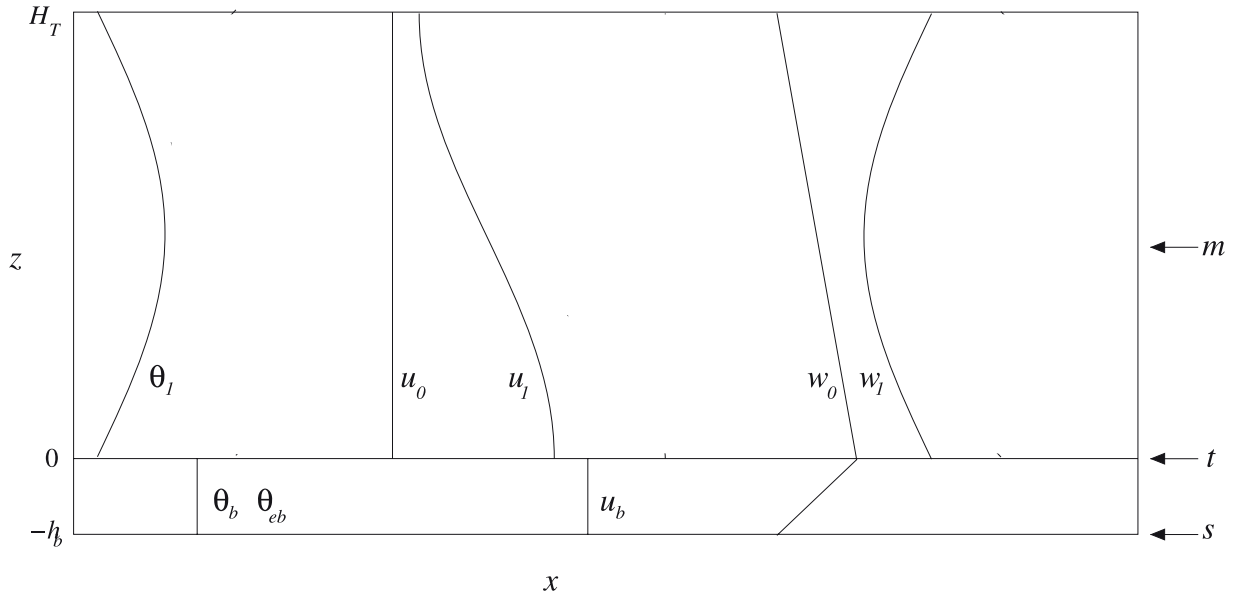

FIG. 4. Schematic diagram of the vertical structures of the atmospheric model variables. The height labels s, t, and m correspond to the surface of the earth, the top of the atmospheric boundary layer, and the mid-troposphere. Adapted from Ref. 41.

II. MODEL DESCRIPTION

In this section, the model equations are described. The basic components of the fluid dynamics are similar to other models [26–32, 41–46] that have used simplified vertical structures as in Fig. 4. The main new aspect here is the inclusion of stochasticity as in recent work [21–25] so that the stochastic models for shallow clouds and cloud clusters are extended to be coupled with radiation and large-scale atmospheric fluid dynamics.

In what follows, the model variables are described in section II A; the evolution equations are described in sections II B, II C, and II D, for the free troposphere, boundary layer, and ocean, respectively; and the numerical methods are described in section II E.

A. Variables and vertical structures

The model variables will have simplified vertical structures, as illustrated in Fig. 4, which brings a substantial savings in computational cost. Note that the functional form of the vertical structures arises systematically from a Sturm–Liouville problem [33], and the simplification (and computational savings) comes from using a superposition of only two vertical modes rather than an infinite sum of vertical modes.

The form of the vertical structures can be derived from a Sturm–Liouville problem associated with the linearized evolution equations,

$$\frac{\partial u_f}{\partial t} + \frac{\partial p_f}{\partial x} = 0, \tag{1}$$

$$\frac{\partial v_f}{\partial t} + \frac{\partial p_f}{\partial y} = 0, \tag{2}$$

$$\frac{\partial p_f}{\partial z} = g\frac{\theta_f}{\theta_f^{ref}}, \tag{3}$$

$$\frac{\partial u_f}{\partial x} + \frac{\partial v_f}{\partial y} + \frac{\partial w_f}{\partial z} = 0, \tag{4}$$

$$\frac{\partial \theta_f}{\partial t} + w_f\frac{\partial \theta_{bg}}{\partial z} = 0, \tag{5}$$

$$\frac{\partial r_f}{\partial t} + w_f\frac{\partial r_{bg}}{\partial z} = 0. \tag{6}$$

The subscript f indicates that the variables are associated with the free troposphere, where the components of the velocity vector are u_f, v_f), and w_f, and the other variables are the (scaled) pressure p_f, potential temperature θ_f, and water vapor mixing ratio q_f. The equations in (1)–(6) are a linearization of the hydrostatic Boussinesq equations, also known as the primitive equations. Evolution equations will be discussed in further detail below. For the moment, the evolution equations are introduced in (1)–(6) to explain the form of the vertical structures. In particular, in seeking solutions of (1)–(6) based on separation of variables, a Sturm–Liouvile problem arises for the vertical structures [33]. Let $G_j(z)$, for $j = 0, 1, 2, 3, \cdots$, denote the vertical basis functions that arise from the Sturm–Liouville problem. A generic variable $\phi(x, y, z, t)$ can then be expressed as an infinite series as

$$\phi(x, y, z, t) = \sum_{j=0}^{\infty} \phi_j(x, y, t)G_j(z), \tag{7}$$

where the functions $\phi_j(x, y, t)$ are the expansion coefficients. For simplified models, it is common to truncate the infinite series after the first terms as, for instance,

$$\phi(x, y, z, t) \approx \phi_0(x, y, t)G_0(z) + \phi_1(x, y, t)G_1(z). \tag{8}$$

These first two terms are called the barotropic mode and the first baroclinic mode, respectively. It is common to consider such a truncation since it embodies the essential features of atmospheric circulations [26–28, 47–51] and since the first terms contain the most variability based on observational data analyses [52, 53]. For a Boussinesq system, the basis functions $G_j(z)$ are sines and cosines [33], as described in further detail next.

In the free troposphere, the three-dimensional velocity vector is partitioned into its two-dimensional horizontal component, $\mathbf{u}_f = (u_f, v_f)$, and its vertical component, w_f, with subscript f to denote the free troposphere. For

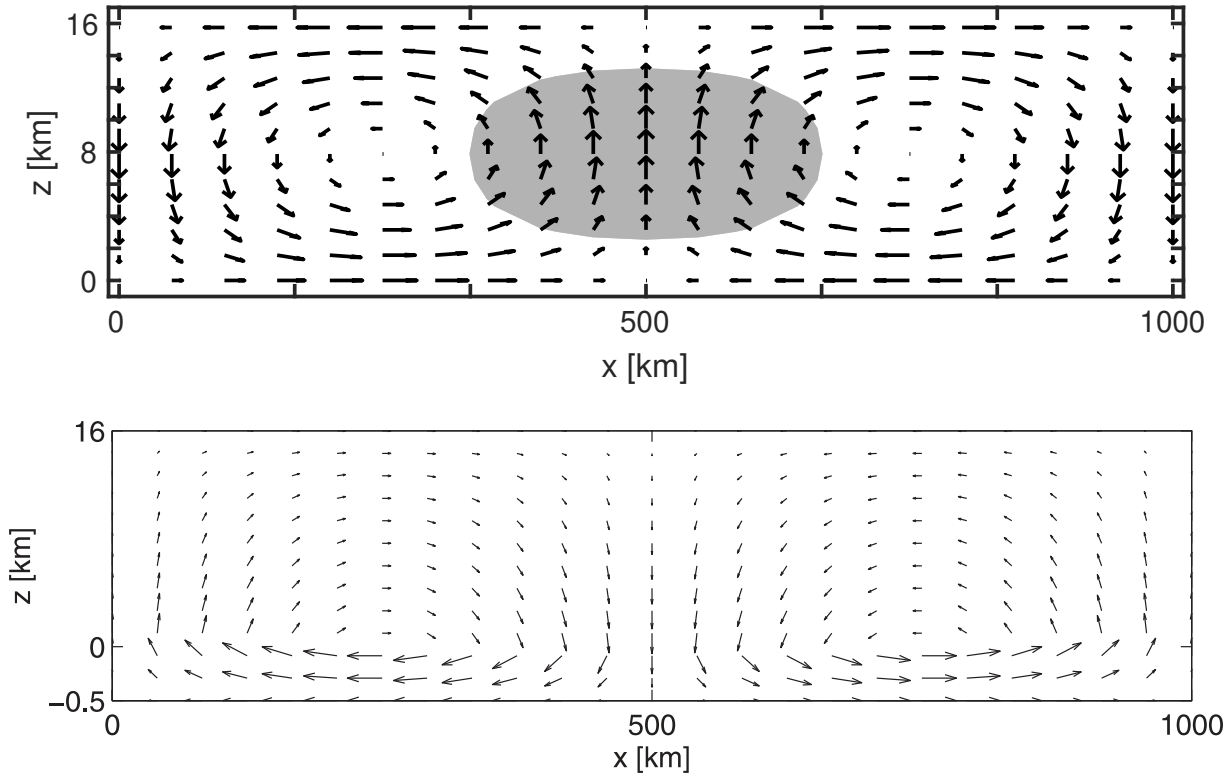

FIG. 5. Illustrations of circulation cells that arise from the vertical structures from Fig. 4. Top: A deep circulation cell arises from u_1 and w_1. Gray shading indicates deep convective clouds associated with upward motion, as in the Walker circulation cells of Fig. 1. Bottom: Boundary-layer convergence from u_b can create a circulation cell in concert with free-tropospheric, barotropic u_0, w_0. Bottom panel is from Ref. 41. © American Meteorological Society. Used with permission.

velocity, the expansion from (8) takes the form

$$\mathbf{u}_f(x,y,z,t) = \mathbf{u}_0(x,y,t) + \mathbf{u}_1(x,y,t)\sqrt{2}\cos\frac{\pi z}{H_T}, \tag{9}$$

$$w_f(x,y,z,t) = w_0(x,y,t)(H_T - z) + w_1(x,y,t)\sqrt{2}\sin\frac{\pi z}{H_T}, \tag{10}$$

where H_T is the depth of the troposphere, and the vertical structures are shown in Fig. 4. For a Boussinesq system, the incompressibility condition of $\partial_x u_f + \partial_y v_f + \partial_z w_f = 0$ leads to the relationships

$$w_0 = \partial_x u_0 + \partial_y v_0, \qquad w_1 = -\frac{H_T}{\pi}(\partial_x u_1 + \partial_y v_1). \tag{11}$$

If an anelastic atmosphere is assumed instead of Boussinesq, then the vertical gradient of density is taken into account, and the vertical structures have a more complicated form [26], although in either case the basic features are the same. One could include additional basis functions [29, 34], such as $\sin(2\pi z/H_T)$ or $\sin(3\pi z/H_T)$, etc., beyond the first baroclinic mode structure $\sin(\pi z/H_T)$ used here, but the largest amount of atmospheric variance is in the first baroclinic mode [52]. As an illustration, if the velocity structures in (9)–(10) are plotted as vector fields, then a sinusoidal variation in x will produce a circulation cell as shown in Fig. 5. The deep circulation cell in Fig. 5 is similar to the Walker circulation cells from Fig. 1, which indicates that the simple vertical structures in (9)–(10) are sufficient to capture the basic aspects of deep convection and atmospheric circulations.

The thermodynamic variables in the free troposphere are the potential temperature, θ_f, and the water vapor mixing ratio, r_f. Their structures take the form

$$\theta_f(x,y,z,t) = \theta_f^{ref} + \theta_{bg}(z) + \theta_1(x,y,t)\sqrt{2}\sin\frac{\pi z}{H_T}, \tag{12}$$

$$r_f(x,y,z,t) = r_0(x,y,t)e^{-z/H_q}, \tag{13}$$

which are similar to (9)–(10). In (12), θ_f^{ref} is a constant reference value, and $\theta_{bg}(z)$ is a background profile, with $\theta_{bg}(0) = 0$ and with $d\theta_{bg}/dz$ a positive constant. In (13), H_q is a decay height for the moisture profile, and r_0 is the value at the top of the boundary layer, $z = 0$. Layer parameters and thermodynamic parameters are listed in Table I, and parameter values of the background states are listed in Table II.

TABLE I. Layer parameters and thermodynamic parameters

parameters	value	unit	description
H_T	16000	m	Tropopause height
h_b	500	m	Atmospheric boundary layer thickness
h_o	10	m	Ocean mixed layer thickness
ρ_o	1000	kg/m^3	Density of ocean water
ρ_b	0.885	kg/m^3	Density of boundary layer air
ρ_f	0.37	kg/m^3	Density of free troposphere air
c_o	4148	J/kg/K	Heat capacity of ocean water
c_p	1005	J/kg/K	Heat capacity of dry air
R_d	287	J/kg/K	Gas constant of dry air
L_v	2.4×10^6	J/kg	Latent heat of vaporization

TABLE II. Parameters of background states

parameters	value	unit	description
H_q	2000	m	Free troposphere moisture scale
Q_0	3.848×10^{-2}	m	Background moisture stratification
Q_1	5.328×10^{-3}	m	Background barotropic vertical moisture advection
T_f^0	258.94	K	Background temperature in T_f
T_f^1	0.6844		Linear dependency of θ_1 in T_f
θ_f^{ref}	300	K	Reference temperature in free troposphere
$d\theta_{bg}/dz$	3	K km^{-1}	Vertical gradient of background potential temperature
$q_{b,sat,0}$	-270	mm	Background column water vapor in $q_{b,sat}$
$q_{b,sat,1}$	1	mm/K	Linear dependency of T_b in $q_{b,sat}$
$q_{f,sat,0}$	-228	mm	Background column water vapor in $q_{f,sat}$
$q_{f,sat,1}$	1	mm/K	Linear dependency of T_f in $q_{f,sat}$
F_o	0.0556	K/day	Forcing strength on ocean temperature

In addition to the mixing ratio r_f, it is also sometimes convenient to work with the column water vapor (CWV), which we denote by q_f and define as

$$q_f(x, y, t) = \frac{\rho_f}{\rho_o} \int_0^{H_T} r_f(x, y, z, t)\, dz, \tag{14}$$

which is the integral of the mixing ratio over the atmospheric column. The density ρ_f is the average density of the atmosphere in the free troposphere, and it could be replaced by a height-dependent $\tilde{\rho}(z)$ and brought inside the integrand, although the version in (14) will serve the present purposes. The parameter ρ_o is the density of liquid water (or ocean water), and one can see that (14) transforms r_f with units of kg water per kg dry air (or kg kg^{-1} for short) to q_f with units of mm. Physically, the CWV q_f represents the height of liquid water that would result if all water vapor in the column were condensed to liquid form.

Since both $r_0(x, y, t)$ from (13) and $q_f(x, y, t)$ from (14) will be useful in different contexts, it is helpful to define the relationship between them. To do so, insert (13) into (14) to find

$$q_f = H_T \hat{Q}_0 \frac{\rho_f}{\rho_o} r_0, \quad \text{with} \quad \hat{Q}_0 = \frac{H_q}{H_T}\big(1 - \exp(-H_T/H_q)\big). \tag{15}$$

For short, we will sometimes refer to the water vapor mixing ratio (r_f or r_0) or the column water vapor as simply the "water" or the "moisture."

In addition to the potential temperature θ_f, it is also useful to define other temperature quantities. The temperature itself will be denoted by T_f^{tot} to indicate that it is the total temperature as opposed to an anomaly, and it is related,

by definition, to potential temperature via

$$T_f^{tot}(x,y,z,t) = \theta_f(x,y,z,t) \cdot \left(\frac{\tilde{p}(z)}{p_0}\right)^{R_d/c_p} \tag{16}$$

where R_d is the gas constant for dry air, c_p is the specific heat at constant pressure, $\tilde{p}(z)$ is the background pressure profile, and p_0 is a reference pressure that is taken to be the surface pressure—i.e., $p_0 = \tilde{p}_f(0)$.

For later use with radiative transfer, with simplified vertical structures, it is convenient to define the mass average of the temperature in the free troposphere, which we will call T_f:

$$T_f = \frac{1}{\int_0^{H_T} \tilde{\rho}(z)dz} \int_0^{H_T} T_f^{tot}(x,y,z,t)\tilde{\rho}(z)dz = T_f^0 + T_f^1 \cdot \theta_1. \tag{17}$$

In the second equality above, the mass-averaged temperature T_f has been related to the first-baroclinic-mode potential temperature θ_1, by evaluating the integral in (17) and using (16) and (12); the constants T_f^0 and T_f^1 arise from the integration. This relationship will be useful later in moving between the variable θ_1, which is useful for the fluid dynamics, and the variable T_f, which is useful for radiative transfer. One other temperature quantity that will be of use later is the equivalent potential temperature,

$$\theta_{ef}(x,y,z,t) = \left(T_f^{tot}(x,y,z,t) + \frac{L_v}{c_p} r_f(x,y,z,t)\right)\left(\frac{p_0}{\tilde{p}(z)}\right)^{R_d/c_p}, \tag{18}$$

where the subscript f indicates that θ_{ef} is the value of θ_e within the free troposphere. In (18), we use a linearization of the exponential function that arises in the more comprehensive definition of $\theta_e \approx \theta \exp[L_v q_v/(c_p T)]$ [8], since the linearization allows simpler transformations between the variables θ_{ef}, T_f^{tot}, and r_f, and is reasonably accurate for present purposes. Of use later on is the value of θ_{ef} at the top of the boundary layer,

$$\theta_{ef}^0(x,y,t) = \theta_f^{ref} + \frac{\tilde{L}_v^f}{c_p}\hat{Q}_0^{-1} q_f, \quad \text{with} \quad \tilde{L}_v^f = \frac{L_v \rho_o}{H_T \rho_f}, \tag{19}$$

which arises from (18) by evaluating at $z = 0$.

In the boundary layer, all variables are height-averaged and therefore independent of height, as illustrated in Fig. 4. The one exception is the vertical velocity, w_b, which is linear-in-height:

$$w_b(x,y,z,t) = -(z + h_b)\nabla \cdot \mathbf{u}_b(x,y,t), \tag{20}$$

where the horizontal divergence $\nabla \cdot \mathbf{u}_b$ appears here so that the velocity field satisfies the divergence-free constraint:

$$\nabla \cdot \mathbf{u}_b + \frac{\partial w_b}{\partial z} = 0. \tag{21}$$

The thermodynamic variables in the boundary layer are analogous to their counterparts in (12)–(18) from the free troposphere. Water will be partitioned into water vapor mixing ratio $r_{vb}(x,y,t)$ and liquid water mixing ratio $r_{lb}(x,y,t)$, and their sum, the total water mixing ratio $r_{tb}(x,y,t)$, where the subscript b denotes the boundary layer. The boundary-layer CWV and column total water are defined as

$$\begin{aligned} q_{vb}(x,y,t) &= \frac{\rho_b}{\rho_o}\int_{-h_b}^{0} r_{vb}(x,y,t)\, dz = h_b \frac{\rho_b}{\rho_o} r_{vb}(x,y,t), \\ q_{tb}(x,y,t) &= \frac{\rho_b}{\rho_o}\int_{-h_b}^{0} r_{tb}(x,y,t)\, dz = h_b \frac{\rho_b}{\rho_o} r_{tb}(x,y,t). \end{aligned} \tag{22}$$

The temperature T_b, potential temperature θ_b, and equivalent potential temperature θ_{eb} are related to each other via

$$T_b(x,y,t) = T_b^{ref} + \theta_b(x,y,t), \tag{23}$$

$$\theta_{eb}(x,y,t) = \left(T_b + \frac{L_v}{c_p} r_{vb}\right)\left(\frac{p_0}{p_b}\right)^{R_d/c_p} = T_b + \frac{\tilde{L}_v^b}{c_p} q_{vb}, \tag{24}$$

where $T_b^{ref} = 300$ K is a constant reference value of the atmospheric temperature near the ocean surface, where we have used $p_b \approx p_0$ in the θ_{eb} definition above, and where $\tilde{L}_v^b$ is a scaled latent heat in the boundary layer, with

$\tilde{L}_v^b = L_v^b/h_b$ and $L_v^b = L_v(\rho_o/\rho_b)$. The definitions for the boundary layer in (22)–(24) are similar to (14)–(18) for the free troposphere.

The presence of clouds will be described by cloud indicator functions σ_f and σ_b for the free troposphere and boundary layer, respectively. To define the presence of a cloud, we compare the moisture value q_f to a threshold value $q_{f,sat}$ and define

$$\sigma_f(x,y,t) = \mathcal{H}(q_f - q_{f,sat}), \qquad \sigma_b(x,y,t) = \mathcal{H}(q_{tb} - q_{b,sat}), \tag{25}$$

where $\mathcal{H}(q)$ is the Heaviside function, so that $\mathcal{H}(q) = 1$ if $q \geq 0$ and $\mathcal{H}(q) = 0$ if $q < 0$, and where similar expressions are used above for both σ_f and σ_b. The threshold or saturation values $q_{b,sat}$ and $q_{f,sat}$ are taken here to be linear functions of temperature:

$$q_{b,sat} = q_{b,sat,0} + q_{b,sat,1}T_b, \qquad q_{f,sat} = q_{f,sat,0} + q_{f,sat,1}T_f, \tag{26}$$

where $q_{b,sat,0}, q_{b,sat,1}, q_{f,sat,0}$, and $q_{f,sat,1}$ are constant parameters. The use of saturation values that are linear in temperature can be viewed as a linearization of the type of saturation mixing ratio that arises from the Clausius–Clapeyron equation of thermodynamics [54]. Alternatively, since these cloud indicators are defined on somewhat large scales, the saturation values could be viewed as empirical definitions that can be defined based on observational data [55]. Note that the values of these parameters ($q_{b,sat,0}, q_{b,sat,1}, q_{f,sat,0}$, and $q_{f,sat,1}$) should tacitly depend on other parameters, such as boundary-layer height h_b and free troposphere height H_T, since q_{tb} and q_f are integrated over these heights, respectively. These cloud indicators will act as nonlinear switches that turn on or off certain physical processes, such as rainfall or cloud–radiation interactions, as described further below.

B. Evolution of free troposphere

Now that the variables have been described above in section II A, the dynamical equations of motion can be presented. The evolution equations for the free troposphere will be described first, followed by the evolution equations for the boundary layer and ocean.

The dynamics of the free troposphere is given by

$$\frac{\partial \mathbf{u}_1}{\partial t} - \alpha_1 \nabla\theta_1 = -\frac{1}{\tau_R}\mathbf{u}_1, \tag{27}$$

$$\frac{\partial \theta_1}{\partial t} - \alpha_2 \nabla \cdot \left(\mathbf{u}_1 - \sqrt{2}\mathbf{u}_0\right) = S_{\theta_1}, \tag{28}$$

for the first-baroclinic-mode velocity $\mathbf{u}_1$ and potential temperature θ_1, and

$$\frac{\partial q_f}{\partial t} + \nabla \cdot \left(Q_1\mathbf{u}_1 - Q_0\mathbf{u}_0\right) = S_{q_f} \tag{29}$$

for the free-tropospheric moisture. The barotropic velocity $\mathbf{u}_0$ will be described further below due to its coupling with the boundary layer. In essence, (27)–(28) describes a shallow-water system for $\mathbf{u}_1(x,y,t)$ and $\theta_1(x,y,t)$, and a similar type of equation for q_f. Note that it is not the same as the traditional, single-layer shallow water equations, but it has connection to multi-mode or multi-layer shallow water equations, as mentioned further below. The fluid flow will be driven by the heat source/sink S_{θ_1}, which is described further below and includes cloud latent heating that is interactive and evolving based on individual cloud clusters.

The left-hand side of (27)–(29) is the dynamical core, and it can be derived from the 3D fluid dynamics equations as follows [26, 28, 29, 33, 34, 46]. The starting point is the hydrostatic primitive equations

$$\frac{\partial u_f}{\partial t} + \frac{\partial p_f}{\partial x} = 0, \tag{30}$$

$$\frac{\partial v_f}{\partial t} + \frac{\partial p_f}{\partial y} = 0, \tag{31}$$

$$\frac{\partial p_f}{\partial z} = g\frac{\theta_f}{\theta_f^{ref}}, \tag{32}$$

$$\frac{\partial \theta_f}{\partial t} + w_f\frac{\partial \theta_{bg}}{\partial z} = 0, \tag{33}$$

$$\frac{\partial r_f}{\partial t} + w_f\frac{\partial r_{bg}}{\partial z} = 0. \tag{34}$$

Note that the hydrostatic assumption is a helpful assumption for deriving simplified equation sets although for grid spacings in the range of $O(1)$ to $O(10)$ km it may not be the complete description of phenomena on the smallest model scales. Also note that nonlinear advection terms have been neglected, while advection of the background state $\theta_{bg}(z)$ is included, and advection of q has been linearized with respect to a background state $r_{bg}(z) = r_{00}\exp(-z/H_q)$. Nonlinear advection could possibly be included in the future [28, 29, 34], although a careful investigation is still needed for the interactions of nonlinear advection and stochasticity in the present type of framework, and numerical methods should therefore be chosen appropriately. Nonlinear advection is presently represented statistically via the eddy diffusion and stochastic forcing in (29) as a parameterization of turbulent advection–diffusion. Some other climate components that will be neglected in the idealized simulations here are spherical geometry of Earth, rotation, and the diurnal cycle, although these and other features could be added in the future.

To derive the shallow water system in (27)–(29), the vertical structures arise from a Sturm–Liouville problem and were described in (9)–(14). It then follows from (12) and from hydrostatic balance in (32) that the vertical structure of the (scaled) pressure is

$$p_f(x,y,z,t) = p_{bg}(z) + p_0(x,y,t) + p_1(x,y,t)\sqrt{2}\cos\frac{\pi z}{H_T}, \qquad p_1 = -\frac{g}{\theta_f^{ref}}\frac{H_T}{\pi}\theta_1. \tag{35}$$

Then the evolution equations in (30)–(34) are projected onto the vertical structures from the Sturm–Liouville problem using the inner product

$$\langle f, g\rangle = \frac{1}{H_T}\int_0^{H_T} f(z)g(z)\,dz. \tag{36}$$

Since the vertical structure functions in (9)–(12) are sines and cosines as in a Fourier series, the projections and inner products are straightforward [28, 29, 33, 34, 46]. By projecting the momentum equations in (30)–(31) onto the basis function $\sqrt{2}\cos(\pi z/H_T)$, one arrives at the shallow-water momentum equations in (27) with $\alpha_1 = gH_T/(\pi\theta_f^{ref}) \approx 170$ m^2 s^{-2} K^{-1}. Similarly, by projecting the θ_f evolution equation in (33) onto the basis function $\sqrt{2}\sin(\pi z/H_T)$, one arrives at the shallow-water θ_1 equation in (28) with $\alpha_2 = (H_T/\pi)(d\theta_{bg}/dz) \approx 15$ K, where $d\theta_{bg}/dz = 3$ K km^{-1} is assumed constant. Finally, for the moisture, the r_f evolution equation in (34) is projected onto a constant function in order to obtain the column water vapor from (14); the result is the shallow-water moisture equation in (29) with

$$\begin{aligned} Q_0 &= -\frac{\rho_f}{\rho_o}\int_0^{H_T}\frac{dr_{bg}}{dz}\big(H_T - z\big)\,dz, \\ Q_1 &= -\frac{\rho_f}{\rho_o}\int_0^{H_T}\frac{dr_{bg}}{dz}\frac{H_T}{\pi}\sqrt{2}\sin\frac{\pi z}{H_T}\,dz, \end{aligned} \tag{37}$$

where recall that $r_{bg}(z) = r_{00}\exp(-z/H_q)$. The values of parameters Q_0 and Q_1 are listed in Table II. Note that the system in (27)–(29) is not the traditional, single-layer shallow water equations, but it can be viewed as one mode of multi-mode shallow water equations if additional vertical basis functions are considered [34]. Also, this connection with shallow water systems can be seen to arise because the primitive equations in (30)–(34) can be viewed as a multi-layer shallow water system; see Ref. 56, chapter 2, sections 18 and 19. This completes the derivation of the dynamical core on the left-hand side of the shallow-water-like system in (27)–(29).

On the right-hand side of (27)–(29) are the source/sink terms, which are interactive and evolving and defined as follows. In the momentum equation, the sink $-\mathbf{u}_1/\tau_R$ is a Rayleigh damping term. In the moisture equation, the source/sink S_{q_f} is defined as

$$S_{q_f} = -\frac{1}{\tau_q}\big[q_f - q_{f,sat}(T_f)\big]^+ + \frac{\sigma_b}{\tau_t}\big(q_{tb} - q_f\frac{h_b\rho_b}{H_T\rho_f}\hat{Q}_0^{-1}\big) + b_q\nabla^2 q_f + D_f\dot{W}_f, \tag{38}$$

and the four terms represent precipitation from deep-convective clouds, a moisture source from cloud-top mixing of boundary-layer clouds, eddy diffusion, and stochastic forcing, respectively. The precipitation term includes a superscript $^+$ that indicates a nonlinear switch, so that precipitation turns on only when q_f exceeds the threshold value $q_{f,sat}$, which is a function of temperature according to (17) and (26). The cloud-top mixing term is proportional to the difference between the water content in the free troposphere and boundary layer, and the cloud indicator σ_b is a coefficient that turns on cloud-top mixing only when boundary-layer clouds are present. The eddy diffusion and stochastic forcing are a parameterization of turbulent advection–diffusion [57–60] and are similar to earlier models of spatiotemporal stochastic clouds. The value of, for instance, the eddy moisture diffusivity b_q may appear to be large when written in units of m^2 s^{-1}, but it is more nearly $O(1)$ in magnitude when written in terms of equatorial

TABLE III. Parameters of physical parameterizations

parameters	value	unit	description
τ_s	6	hours	Sensible heating time scale
τ_m	8	hours	Momentum entrainment time scale
τ_q	12	hours	Convection time scale
τ_t	6	days	Cloud top mixing time scale
τ_e	6	days	Sea surface evaporation time scale
τ_R	75	days	Rayleigh drag time scale
C_d	0.025		Surface drag coefficient
U_p	2	m/s	Strength of turbulent coefficient
$\tilde{D}_b$	3.67	$\mathrm{m}/\sqrt{\mathrm{s}}$	Stochastic strength in q_{tb}
$\tilde{D}_f$	1.84	$\mathrm{m}/\sqrt{\mathrm{s}}$	Stochastic strength in q_f
b_v	6.25×10^2	m^2/s	Eddy viscosity
b_T	6.25×10^2	m^2/s	Eddy diffusivity in temperatures
b_q	6.25×10^5	m^2/s	Eddy diffusivity in moisture

synoptic scales, and its value was calibrated based on the power spectrum from observational data [21, 46]. The stochastic forcing $\dot{W}_f$ is a spatiotemporal white noise with mean zero and covariance $E[\dot{W}_f(x,y,t)\dot{W}_f(x',y',t')] = \delta(x-x')\delta(y-y')\delta(t-t')$, or a discretized version as described below in section II E. The values of the parameters from the source/sink terms are listed in Table III.

Note that parameters of various types have been defined here, ranging from fundamental constants of nature such as c_p and L_v in Table I to parameters from physical parameterizations in Table III. For the parameters that are related to physical parameterizations, such as cloud and precipitation processes, the values of the parameters are chosen to be in line with other studies and observational constraints (see, e.g., Refs. 22 and 36 and references therein). Sensitivity studies have also been carried out for many of these parameters and presented in other studies (e.g., Refs. 22 and 36), and some additional sensitivity studies are presented below. While many parameters appear in the present idealized modeling framework, it is a relatively small number of parameters in comparison to comprehensive models such as LES, CRMs, and GCMs, since comprehensive models account for additional aspects, such as cloud microphysics and varying structures in the vertical direction, which require additional parameters [2, 61].

As the last part of the shallow-water system, in the shallow-water equation for θ_1 in (28), the heat source/sink term is given by

$$\begin{aligned} S_{\theta_1} = &\frac{\pi}{2\sqrt{2}}\frac{h_b}{H_T}\frac{\sigma_b}{\tau_t}\left(\theta_{eb} - \theta^0_{ef}\right) - \frac{\pi}{2\sqrt{2}}\frac{\tilde{L}^f_v}{c_p}\frac{\sigma_b}{\tau_t}\left(q_{tb} - q_f\frac{h_b\rho_b}{H_T\rho_f}\hat{Q}_0^{-1}\right) \\ &+ \frac{1}{\tau_q}\cdot\frac{\tilde{L}^f_v}{c_p}\left[q_f - q_{f,sat}(T_f)\right]^+ + \frac{1}{C_f}F_{rad,f}, \end{aligned} \tag{39}$$

where $C_f = c_p\rho_f H_T$ is a scaled version of the specific heat capacity. The first two terms represent the effects of boundary layer cloud-top mixing of equivalent potential temperature and water, respectively, defined below in section II C. The third term is the cloud latent heating that is associated with precipitation in (29), and the coefficient $\tilde{L}^f_v/c_p$ is a latent heating factor, defined above in (19). Note that no stochastic forcing term was included for potential temperature in (39), for simplicity, whereas stochastic forcing was included for moisture in (38); additional stochastic forcing terms could be included, although they would increase the complexity of the model via the introduction of additional parameters and their calibration, and prior work has suggested that the minimal addition of stochasticity to only the moisture equation is sufficient for generating reasonable variability [46]. The fourth term is radiative heating/cooling; it is given by

$$\begin{aligned} F_{rad,f} = &S(1-A_f\sigma_f)a_{sf} + S(1-A_f\sigma_f)(1-a_{sf})a_{sf}A_b\sigma_b \\ &+ a_{lf}a_{lb}\sigma T_b^4 + a_{lf}(1-a_{lb})\sigma T_o^4 - 2a_{lf}\sigma T_f^4, \end{aligned} \tag{40}$$

and it is composed of five terms: absorption of downwelling solar radiation ($\propto S$), absorption of upwelling solar radiation that has reflected off of boundary layer clouds ($\propto S\sigma_b$), absorption of longwave radiation that was emitted by the boundary layer ($\propto \sigma T_b^4$) and ocean ($\propto \sigma T_o^4$), and emission of longwave radiation ($\propto \sigma T_f^4$), respectively. The radiative parameters are the solar constant S (averaged over a diurnal cycle); the Stefan–Boltzmann constant σ; the albedos A_f and A_b of deep convective and boundary layer clouds, respectively; the shortwave absorptivities a_{sf} and a_{sb} of the free troposphere and boundary layer, respectively; and the longwave absorptivities a_{lf} and a_{lb} of the

free troposphere and boundary layer, respectively. The physical interpretation of the first solar radiation term, for instance, is that it represents a fraction of S that is absorbed by the free troposphere, after a fraction $1 - A_f\sigma_f$ is reflected at cloud-top by deep convective clouds in the free troposphere. The absorptivity a_{sf} defines the fraction of incoming radiation that is absorbed by the free troposphere. Further details of the radiation scheme are described in Ref. 36, which has been extended here in a straightforward way to include the effects of an evolving free troposphere and deep convective clouds.

Cloud–radiative feedbacks and water vapor feedback are included the radiation scheme in (40). As mentioned above, A_f and A_b are the albedos of deep convective and boundary layer clouds, respectively. Notice that these albedos always appear along with cloud indicators as $A_f\sigma_f$ and $A_b\sigma_b$, so that cloud–radiative feedback is turned on only when a cloud is present. Water vapor feedback is present in (40) through the absorptivities, a_{lf} and a_{lb}, which are defined as

$$\begin{aligned} a_{lf} &= a_{lf}^0 + a_{lf}^1\left[\frac{q_f}{q_{f,sat}} + \sigma_f\big(1 - \frac{q_f}{q_{f,sat}}\big)\right], \\ a_{lb} &= a_{lb}^0 + a_{lb}^1\left[\frac{q_{vb}}{q_{b,sat}} + \sigma_b\big(1 - \frac{q_{vb}}{q_{b,sat}}\big)\right]. \end{aligned} \tag{41}$$

These absorptivities will increase when the water vapor content increases, since water vapor is a greenhouse gas, and the effect is capped at a maximum value upon cloud formation. The parameter values for radiation are listed in Table IV.

TABLE IV. Radiation parameters.

parameter	value	unit	physical description
S	436	W m^{-2}	Solar flux at top of free troposphere
σ	5.67×10^{-8}	W m^{-2} K^{-4}	Stefan-Boltzmann constant
A_c	0.6		Albedo of shallow cloud
A_f	0.4		Albedo of deep cloud
a_{sb}	0.1		Shortwave absorptivity of boundary layer
a_{sf}	0.25		Shortwave absorptivity of free troposphere
a_{lb}^0	0.24		Longwave absorptivity of boundary layer (dry air)
a_{lb}^1	0.66		Longwave absorptivity of boundary layer (water vapor)
a_{lf}^0	0.4		Longwave absorptivity of free troposphere (dry air)
a_{lf}^1	0.5		Longwave absorptivity of free troposphere (water vapor)

C. Evolution of boundary layer and barotropic mode

For the atmospheric boundary layer, the velocity $\mathbf{u}_b$ is coupled to the barotropic velocity $\mathbf{u}_0$ of the free troposphere as

$$\frac{\partial \mathbf{u}_b}{\partial t} + \frac{1}{\rho_{ref}}\nabla p_b = -\frac{\sigma_b}{h_b\tau_t}\big(\mathbf{u}_b - (\mathbf{u}_0 + \sqrt{2}\mathbf{u}_1)\big) - \frac{C_d U_p}{h_b}\mathbf{u}_b, \tag{42}$$

$$\frac{\partial \mathbf{u}_0}{\partial t} + \frac{1}{\rho_{ref}}\nabla p_0 = \frac{\sigma_b}{H_T\tau_t}\big(\mathbf{u}_b - (\mathbf{u}_0 + \sqrt{2}\mathbf{u}_1)\big), \tag{43}$$

$$h_b\nabla\cdot\mathbf{u}_b + H_T\nabla\cdot\mathbf{u}_0 = 0, \tag{44}$$

$$p_0 = p_b + \sqrt{2}\theta_1 + \frac{\pi}{2}\frac{h_b}{H_T}\theta_b, \tag{45}$$

where θ_b is the anomalous potential temperature in the boundary layer. In this coupling, divergence in the boundary layer is coupled with convergence in the barotropic mode in the free troposphere, as defined in (44) and following earlier work [41, 42]. Also, as illustrated in Fig. 4, at the top of the boundary layer, the vertical velocity is continuous. The pressure relationship in (45) is also a continuity condition at the top of the boundary layer. Taken together, the dynamical core of (42)–(45) involves two pressure variables, p_b and p_0, although the pressure variables are related to each other, which leaves one pressure quantity to be associated with the single incompressibility condition in (44). Also, recall from section II A that all boundary-layer variables are depth-averaged and therefore are functions of x, y, and t.

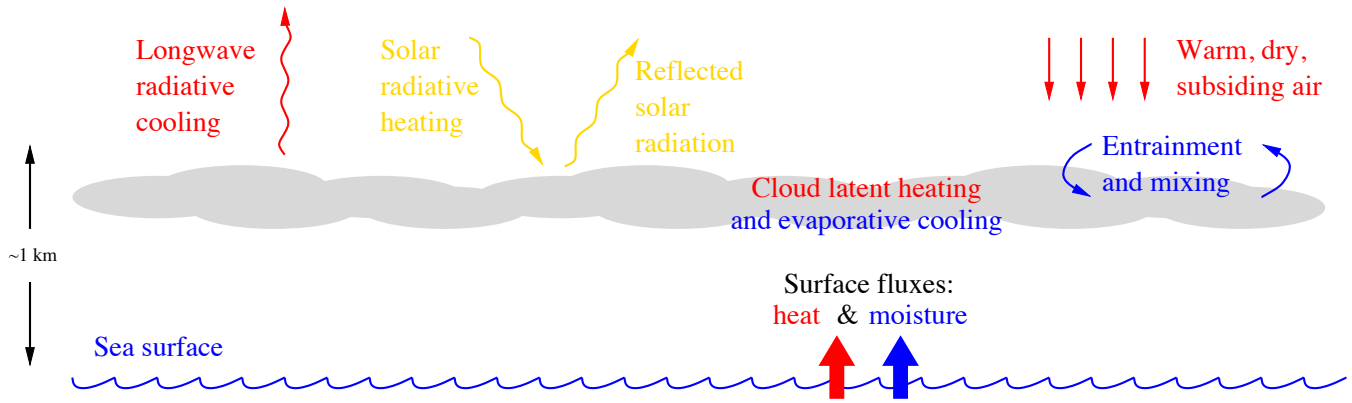

FIG. 6. Schematic diagram of the physical processes related to the atmospheric boundary layer, including interactions with the ocean, free troposphere, and radiation. From [36]. Used with permission.

The source terms in (42)–(43) are related to mixing, drag, and dissipation. The surface drag in the boundary layer is $-(C_d U_p/h_b)\mathbf{u}_b$, where U_p is a measure of turbulent velocity strength and C_d is the non-dimensional surface drag coefficient. The source terms proportional to σ_b are a representation of momentum entrainment at the top of the boundary layer. They are functions of the difference in velocity between the boundary layer ($\mathbf{u}_b$) and the bottom of the free troposphere ($z = 0$), where the velocity $\mathbf{u}_f$ takes the value $\mathbf{u}_0 + \sqrt{2}\mathbf{u}_1$ and has contributions from both the baroclinic mode $\mathbf{u}_1$ and barotropic mode $\mathbf{u}_0$.

For the thermodynamic variable evolution in the boundary layer, two quantities are used: total water mixing ratio q_{tb} and equivalent potential temperature θ_{eb}. The evolution of q_{tb} is given by

$$\frac{\partial q_{tb}}{\partial t} = \frac{1}{\tau_e}\big(q_{b,sat}(T_o) - q_{tb}\big) - \frac{\sigma_b}{\tau_t}\Big(q_{tb} - \frac{h_b\rho_b}{H_T\rho_f} q_f \cdot \hat{Q}_0^{-1}\Big) + b_q\nabla^2 q_{tb} + D_b\dot{W}_b. \tag{46}$$

Fig. 6 is a schematic illustration of the physical processes of the boundary layer. The first term on the right-hand side of (46) represents surface evaporation, and it is a source of moisture for the boundary layer. The second term is proportional to σ_b and represents a transfer of moisture from the boundary layer to the free troposphere via cloud-top mixing. It is proportional to the difference in mixing ratio values between the boundary layer and free troposphere at the top of the boundary layer ($z = 0$). This mixing term also introduced an associated moistening term for the free troposphere in (38) and an associated cooling term for the free troposphere in (39), under the assumption that boundary layer cloud liquid water will evaporate upon mixing into the free troposphere. The last two terms on the right-hand side of (46) are a stochastic representation of turbulent advection–diffusion of moisture, as in Ref. 22 and also used for free tropospheric moisture in (29).

The evolution of the equivalent potential temperature in the boundary layer, θ_{eb}, is given by

$$\frac{\partial \theta_{eb}}{\partial t} = -\frac{\sigma_b}{\tau_t}\big(\theta_{eb} - \theta^0_{ef}\big) + \frac{1}{\tau_s}\big(T_o - \theta_b\big) + \frac{1}{\tau_e}\cdot\frac{\tilde{L}^b_v}{c_p}\big(q_{b,sat}(T_o) - q_{tb}\big) + \frac{1}{C_b}F_{rad,b}, \tag{47}$$

where $C_b = c_p\rho_b h_b$ is a scaled version of the specific heat capacity. The first term on the right-hand side represents cloud-top mixing; it turns on only when a boundary layer cloud is present (i.e., when $\sigma_b = 1$), and it is proportional to the difference between θ_{eb} and θ^0_{ef}, which is the free-tropospheric value of equivalent potential temperature at the top of the boundary layer ($z = 0$), as defined in (19). The second term is sensible heat transfer from the ocean, and it is proportional to the difference between ocean temperature T_o and boundary-layer temperature or potential temperature θ_b. The third term is due to evaporation of water at the ocean surface, as also included in (46), and where $\tilde{L}^b_v = (L_v/h_b)(\rho_o/\rho_b)$ here is a scaled version of the latent heat of vaporization. The fourth term is due to radiation and is given by

$$F_{rad,b} = S(1 - A_f\sigma_f)(1 - a_{sf})(1 - A_b\sigma_b)a_{sb} + a_{lf}a_{lb}\sigma T_f^4 + a_{lb}\sigma T_o^4 - 2a_{lb}\sigma T_b^4, \tag{48}$$

with terms that are similar to the free tropospheric radiation terms in (40). In particular, note that cloud feedbacks enter via $A_f\sigma_f$ and $A_b\sigma_b$, and water vapor feedback enters through the absorptivities a_{lf} and a_{lb}, which were defined in (41).

Note that the radiation scheme is formulated for simplicity in its definition, which is useful for ease of understanding the details of the model formulation. On the other hand, the simple formulation brings complications for comparisons

with other models, which commonly use more comprehensive radiation schemes. For example, in climate-change experiments, it is common to change the concentration of carbon dioxide, which may be straightforward in a comprehensive radiation scheme, but which is less straightforward for a simplistic radiation scheme as used here, where the concentration of carbon dioxide is represented in a hitherto unspecified way through its influence on the absorptivity parameters a_{lb} and a_{lf}. By specifying these types of relationships between physically observed quantities and model parameters, one could pursue in the future a more quantitative comparison between the present idealized framework and more comprehensive model results.

D. Evolution of ocean temperature

Finally, the ocean temperature evolves according to

$$\frac{\partial T_o}{\partial t} = -\frac{1}{\tau_e} \cdot \frac{\tilde{L}_v^o}{c_o}\big(q_{b,sat}(T_o) - q_{tb}\big) - \frac{1}{\tau_s} \cdot \frac{C_b}{C_o}\big(T_o - T_b\big) + F_{merid,o} + \frac{1}{C_o} F_{rad,o}, \tag{49}$$

where $\tilde{L}_v^o = L_v/h_o$ is a scaled version of the latent heat of vaporization, and $C_o = c_o \rho_o h_o$ is a scaled version of the specific heat capacity. This type of model is sometimes called a slab ocean model since it describes the oceanic mixed-layer as a slab that interacts thermodynamically and radiatively with the atmosphere above it. A schematic diagram is shown in Fig. 6 to illustrate the physical processes of the ocean and the atmospheric boundary layer. The four terms on the right-hand side of (49) correspond to the physical processes of evaporation, sensible heat transfer, meridional heat transport, and radiation, respectively. Evaporation and sensible heat transfer typically cause a loss of heat in the ocean, whereas radiation is typically a heat source. The meridional heat transport is defined as

$$F_{merid,o} = F_o \sin \frac{2\pi x}{L_x}, \tag{50}$$

where L_x is the length of the domain in the x direction, and the value of parameter F_o is given in Table II. Following earlier work [62], the prescribed meridional heat transport $F_{merid,o}$ is used to represent the effects of oceanic circulations in nature. The radiation term takes the form

$$F_{rad,o} = S(1-a_{sf})(1-a_{sb})(1-A_f\sigma_f)(1-A_b\sigma_b) + a_{lf}(1-a_{lb})\sigma T_f^4 + a_{lb}\sigma T_b^4 - \sigma T_o^4, \tag{51}$$

and it is composed of four terms: absorption of solar radiation ($\propto S$), absorption of longwave radiation that was emitted by the free troposphere ($\propto \sigma T_f^4$) and boundary layer ($\propto \sigma T_b^4$), and emission of longwave radiation ($\propto \sigma T_o^4$), respectively. The physical interpretation of the solar radiation term, for instance, is that it represents a fraction of S that reaches the ocean surface, after a fraction $1 - A_f\sigma_f$ is reflected by deep convective clouds in the free troposphere, a fraction $1 - a_{sf}$ is absorbed by the free troposphere, a fraction $1 - A_b\sigma_b$ is reflected by boundary layer clouds, and a fraction $1 - a_{sb}$ is absorbed by the atmospheric boundary layer. Further details of the radiation scheme are described in Ref. 36, which has been extended here in a straightforward way to include the effects of an evolving free troposphere and deep convective clouds.

E. Numerical methods

The evolution equations of the model are (27)–(29), (42)–(45), (46), (47), and (49), and they are solved numerically using an operator splitting method. The splitting involves three parts. The first part is the fluid dynamical core,

which is

$$\frac{\partial \mathbf{u}_1}{\partial t} - \alpha_1 \nabla \theta_1 = -\frac{1}{\tau_R}\mathbf{u}_1, \tag{52}$$

$$\frac{\partial \theta_1}{\partial t} - \alpha_2 \nabla \cdot \left(\mathbf{u}_1 - \sqrt{2}\mathbf{u}_0\right) = 0, \tag{53}$$

$$\frac{\partial q_f}{\partial t} + \nabla \cdot \left(Q_1 \mathbf{u}_1 - Q_0 \mathbf{u}_0\right) = 0 \tag{54}$$

$$\frac{\partial \mathbf{u}_b}{\partial t} + \frac{1}{\rho_{ref}} \nabla p_b = -\frac{C_d U_p}{h_b}\mathbf{u}_b, \tag{55}$$

$$\frac{\partial \mathbf{u}_0}{\partial t} + \frac{1}{\rho_{ref}} \nabla p_0 = 0, \tag{56}$$

$$h_b \nabla \cdot \mathbf{u}_b + H_T \nabla \cdot \mathbf{u}_0 = 0, \tag{57}$$

$$p_0 = p_b + \sqrt{2}\theta_1 + \frac{\pi}{2}\frac{h_b}{H_T}\theta_b, \tag{58}$$

with q_{tb}, θ_{eb}, and T_o held fixed. This fluid dynamical core is a linear, constant–coefficient system, and it can be solved semi-analytically using the Fourier transform. It is semi-analytical rather than analytical only because a numerical Fourier transform is used and because the eigenvalues and eigenvectors of the linear system are found numerically. The time integration can be solved analytically without the need for a numerical integration in time. To eliminate the constraints in (57)–(58), we use a Helmholtz decomposition to replace $\mathbf{u}_b$ and $\mathbf{u}_0$ by streamfunction and velocity potential variables. In other words, rather than using (55)–(56) directly, we use the divergence and curl of (55)–(56), written in terms of streamfunction and velocity potential.

The second part of the splitting is the stochastic representation of turbulent advection–diffusion from (29) and (46),

$$\frac{\partial q_f}{\partial t} = b_q \nabla^2 q_f + D_f \dot{W}_f, \tag{59}$$

$$\frac{\partial q_{tb}}{\partial t} = b_q \nabla^2 q_{tb} + D_b \dot{W}_b, \tag{60}$$

which evolves q_f and q_{tb} while holding all other variables fixed. For this part of the evolution, a Fourier transform is used, and (59)–(60) becomes a system of independent Ornstein–Uhlenbeck processes that can be solved analytically [21, 63].

Lastly, the third part of the splitting includes all of the other terms in the system, which are mostly interactive source/sink terms such as radiation, etc., and which are a system of ordinary differential equations (ODEs) at each (x, y) location. As a numerical integration scheme, the forward Euler method was used, in line with the first-order splitting scheme. This method offers computational efficiency, which is advantageous for the present goal of long-time simulations of climate.

The domain size here is 10,000 km in the zonal (x) direction and 400 km in the meridional (y) direction. These choices allow the model to represent one branch of the global Walker circulation, such as the circulation cell over the Pacific ocean, and also to represent mesoscale convective systems as stochastic cloud clusters. Doubly periodic boundary conditions are used in the x and y directions. Alternatively, another reasonable choice for boundary conditions could be a channel domain with boundaries at the north and south edges of the domain. One disadvantage of channel boundaries is that the simulation features may be influenced by the boundaries, and the region near the boundary may need to be neglected when calculating statistics. For this reason, periodic boundary conditions can be desirable instead, since the statistics are homogeneous in space and are not influenced by any boundaries. The grid spacing is $\Delta x = \Delta y = 5$ km, which is chosen to be the same as in earlier studies with spatiotemporal stochastic models for clouds [21, 22]. The time step is $\Delta t = 1$ minute, and it is chosen to resolve all time scales involved in the system, including wave oscillation time scales and physical parameterization time scales. As a brief summary of the analysis of all such time scales, it is the wave oscillations that are the limiting factor, or possibly eddy diffusion if the eddy diffusivity is large. The wave propagation speed of the first baroclinic mode $(\mathbf{u}_1, \theta_1)$ is roughly $c_{wave} \approx 50$ m/s, so that the time step should be smaller than roughly $\Delta x / c_{wave} \approx 100$ s. With such a time step, to simulate 2 years of weather and climate evolution will require roughly 10^6 time steps.

The initial conditions are chosen to be near a climate equilbrium state, in order to help reach a statistical equilibrium with a minimal amount of transient spin-up time. The initial guess for a climate equilibrium state is based on an earlier version of the model [36] which was spatially uniform. In particular, the spatially uniform component of the initial conditions is $T_o = 300$ K, $T_b = 290$ K, $T_f = 265$ K, $q_f = 10$ mm, and $q_{tb} = 25$ mm, and other variables are either derived from these or are set to zero. On top of this spatially uniform component is a spatially varying

perturbation, which helps to initiate waves, cloud clusters, and other weather fluctuations. The spatially varying perturbations were chosen with large-scale wavelengths in both the x and y directions, and with randomly selected amplitudes. For the ocean temperature, the spatially varying perturbation was chosen to have a form that is similar to the prescribed ocean heat transport/forcing term, $F_{merid,o}(x)$.

The computer code used here is written in the Fortran programming language, and it is parallelized using message passing interface (MPI). It is based on an earlier parallel code that solves the stochastic heat equation or the quasi-geostrophic (QG) equations using domain decomposition [64].

Spatiotemporal white noise terms, of the form $D\dot{W}(x,y,t)$ with strength parameter D, are included in (59)–(60). For a continuum model, it is well-known that the stochastic heat equation with spatiotemporal white noise forcing will not generate an evolution with finite variance in two spatial dimensions; as a result, to obtain an evolution with finite variance, $\dot{W}(x,y,t)$ must be regularized or discretized. Here we discretize $D\dot{W}(x,y,t)$ in the natural way as $\tilde{D}\dot{W}_{ij}(t)$, which is an independent white noise at each grid point (x_i, y_j), and where $\tilde{D} = D/(\Delta x \Delta y)^{1/2}$. By scaling $\tilde{D}$ with factors of $\Delta x^{1/2}$ and $\Delta y^{1/2}$, the covariance of $\tilde{D}\dot{W}_{ij}(t)$ will approximate the covariance of $D\dot{W}(x,y,t)$.

III. NUMERICAL SIMULATIONS

Numerical simulations are now presented to investigate the level of realism in the idealized climate system and changes under global warming. The standard parameter values used here are listed above in Tables I–IV, and other aspects of the setup of the simulations were described above in section II E.

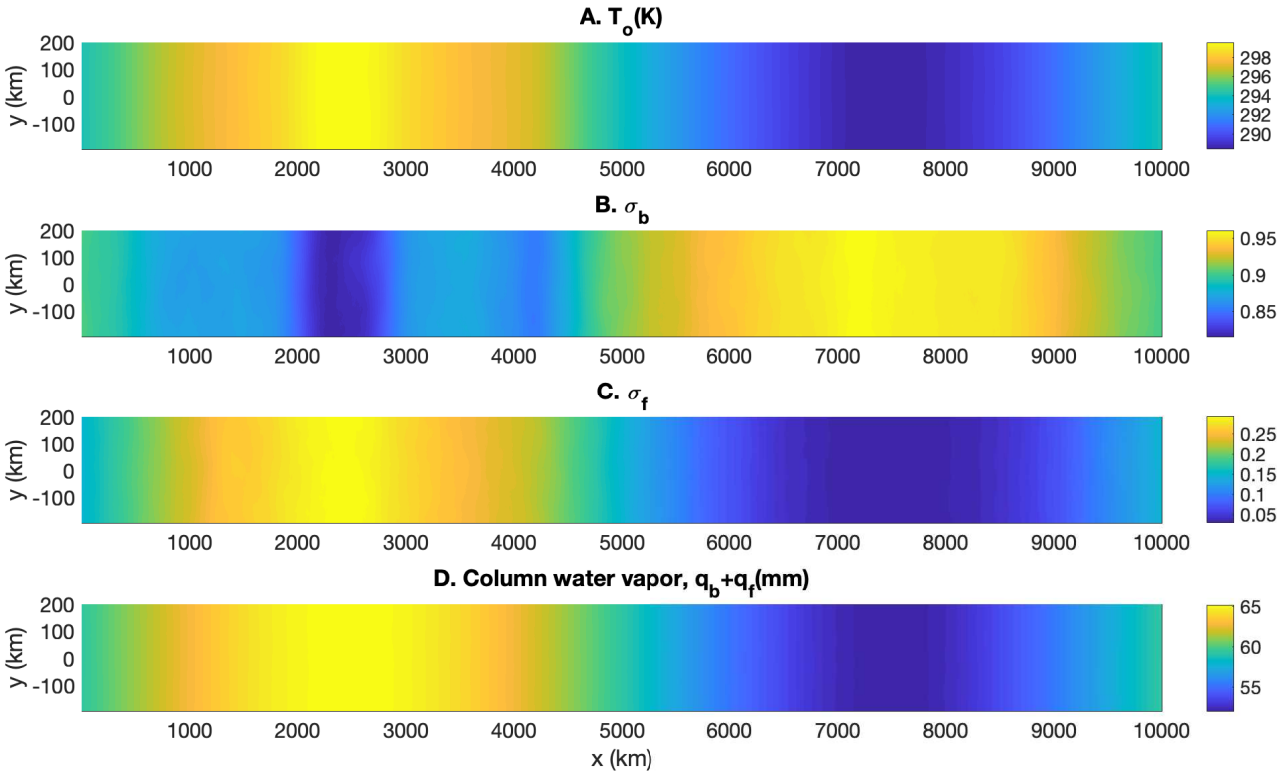

FIG. 7. The mean climate state (i.e., time-averaged quantities) from the simulation with standard parameters. (A) Ocean temperature. (B) Shallow cloud fraction, from boundary-layer cloud indicator, σ_b. (C) Deep convective cloud fraction, from free-tropospheric cloud indicator, σ_f. (D) Column water vapor, from summation of q_{tb} and q_f.

The mean climate state is illustrated in Fig. 7. The simulation was run for 10 years, and the first 7 years involve a transient spin-up period, followed by the final 3 years that are in an approximate statistical equilibrium. By calculating time averages over the final 3 years, the mean climate state in Fig. 7 is obtained. First, in Fig. 7A, the ocean temperature is shown, and it illustrates the warm pool in the western side of the domain and the cold pool in

the eastern side of the domain, which arises from the model's meridional ocean heat transport and is an idealization of the sea surface temperature distribution of the tropical/subtropical Pacific Ocean. The other features of the mean climate state are also in the form of idealizations of the tropical/subtropical Pacific Ocean climate, with a western warm pool region that has excess moisture and deep convection, and an eastern cold pool region that has a dearth of moisture and deep convection. In more detail, some of the values are in reasonable agreement with nature, such as warm-pool ocean temperatures of roughly 300 K and column water vapor of roughly 65 mm (see, e.g., Ref. 55). On the other hand, some values are not in agreement with nature, such as the large value for shallow cloud fraction[1] of 0.8 in the warm pool region, and they could indicate aspects where parameter changes or parameterization changes would be beneficial. For shallow cloud fraction in Fig. 7B, the eastern cold pool region has a cloud fraction of roughly 0.95 and is an idealization of a stratocumulus cloud deck. In summary, the simulation displays some of the basic features of the tropical/subtropical Pacific Ocean climate, in idealized form.

Cloud structures are illustrated in white color in Fig. 8. Two example snapshots are shown, at times of 8 years and 10 years, for each of the two cloud indicators: the boundary-layer cloud indicator, σ_b, in panels A and B, and the free-tropospheric (deep) cloud indicator, σ_f, in panels C and D. In order to fit the plots on the page in a way that illustrates the cloud structures, the domain has been rotated counterclockwise by 90°. As a result, the top of the page is the location of the eastern cold pool region, and the bottom of the page is the location of the western warm pool region.

The shallow clouds cover almost the entire eastern cold pool region (top of the page) in Fig. 8A,B. This is an idealization of a stratocumulus cloud deck, as in earlier versions of spatiotemporal stochastic cloud models for shallow clouds [22]. The shallow clouds dissipate and break up over many portions of the western warm pool (bottom of the page), where many regions are black in color, indicative of the ocean surface and the absence of clouds. The shallow cloud fraction in the warm pool region is larger here in this idealized climate system than in nature, as mentioned above along with a caveat about comparisons with observational analyses, and the cloud fraction could change depending on various factors. Overall, these snapshots illustrate that the model framework is able to produce spatiotemporal variations in shallow clouds, and also in the regional extents of shallow cloud coverage.

Cloud clusters of various sizes can be seen in the deep convective cloud indicator σ_f in Fig. 8C,D. While deep convection is most active over the western warm pool region (bottom half of page), deep convective clouds can occur intermittently in the eastern cold pool region as well (top half of the page), although they are rare enough that the average deep convective cloud fraction is nearly zero over the eastern cold pool (Fig. 7C). The sizes of the cloud clusters can vary substantially, as in earlier versions of spatiotemporal stochastic cloud models [21] and observational data [65]. Many clusters have small length scales of roughly $O(10)$ km, whereas a few clusters have large length scales of roughly $O(100)$ km and extend over a large portion of the 400-km span of the domain in the meridional direction. This ability to represent cloud clusters is one of the advantageous features of the present model framework, in comparison to other models, such as traditional GCMs, that require a larger grid spacing to simulate climate over planetary scales.

The interannual variability is illustrated by the space–time evolution plot in Fig. 9. The same model variables as in Fig. 7 are plotted, and they are plotted for the last two years of the simulation, with all variables averaged over the meridional (y) direction. From this plot, one can see that the climate state is not a fixed, steady equilibrium state but a statistical equilibrium with variability and dynamic evolution. For instance, in panel A, the ocean temperature T_o has fluctuations in time, including fluctuations within the warm-pool region in the western side of the domain. The other variables (in panels A, B, and C) also have substantial fluctuations, including fluctuations in cloud fraction that cover the full range of values from 0 to 1.

Next, a climate-change experiment is performed to investigate the sensitivity of temperature and clouds to an increase of carbon dioxide content. We set up a scenario of enhanced carbon dioxide by increasing the longwave absorptivity of both the boundary layer and free troposphere, following Ref. 36. Specifically, the absorptivity parameters a_{lb}^0 and a_{lf}^0 were increased by a factor of 1.2 to bring them to their new values of $a_{lb}^0 = 0.288$ and $a_{lf}^0 = 0.48$. All other parameters were left unchanged, and a new simulation was run with the same setup as the standard simulation.

In the climate-change simulation, the mean climate state has changed in several ways, as illustrated in Fig. 10. Broadly speaking, figure panels A and C show that with increased carbon dioxide concentration, we would have a warmer ocean and more moisture in the warm-pool region, in comparison to the standard simulation from Fig. 7. For instance, the ocean temperature over the warm pool increased from 300 K to 304 K, and the maximum value of column water vapor has increased from roughly 65 to roughly 70 mm.

The deep convection also undergoes substantial changes in the climate-change simulation. In Fig. 10C a larger cloud fraction of 0.4 is seen over the warm pool, in comparison to 0.3 in the standard simulation, which indicates

[1] Note that the model's cloud indicator quantity σ_b may differ from the shallow cloud or low cloud indicators that are often presented in analyses of observational data, since σ_b could be activated here even when a deep convective cloud is simultaneously present, which is a scenario that would be labeled as deep convective rather than low cloud in some observational analyses. Hence σ_b here could provide an overestimate of low cloud amount.

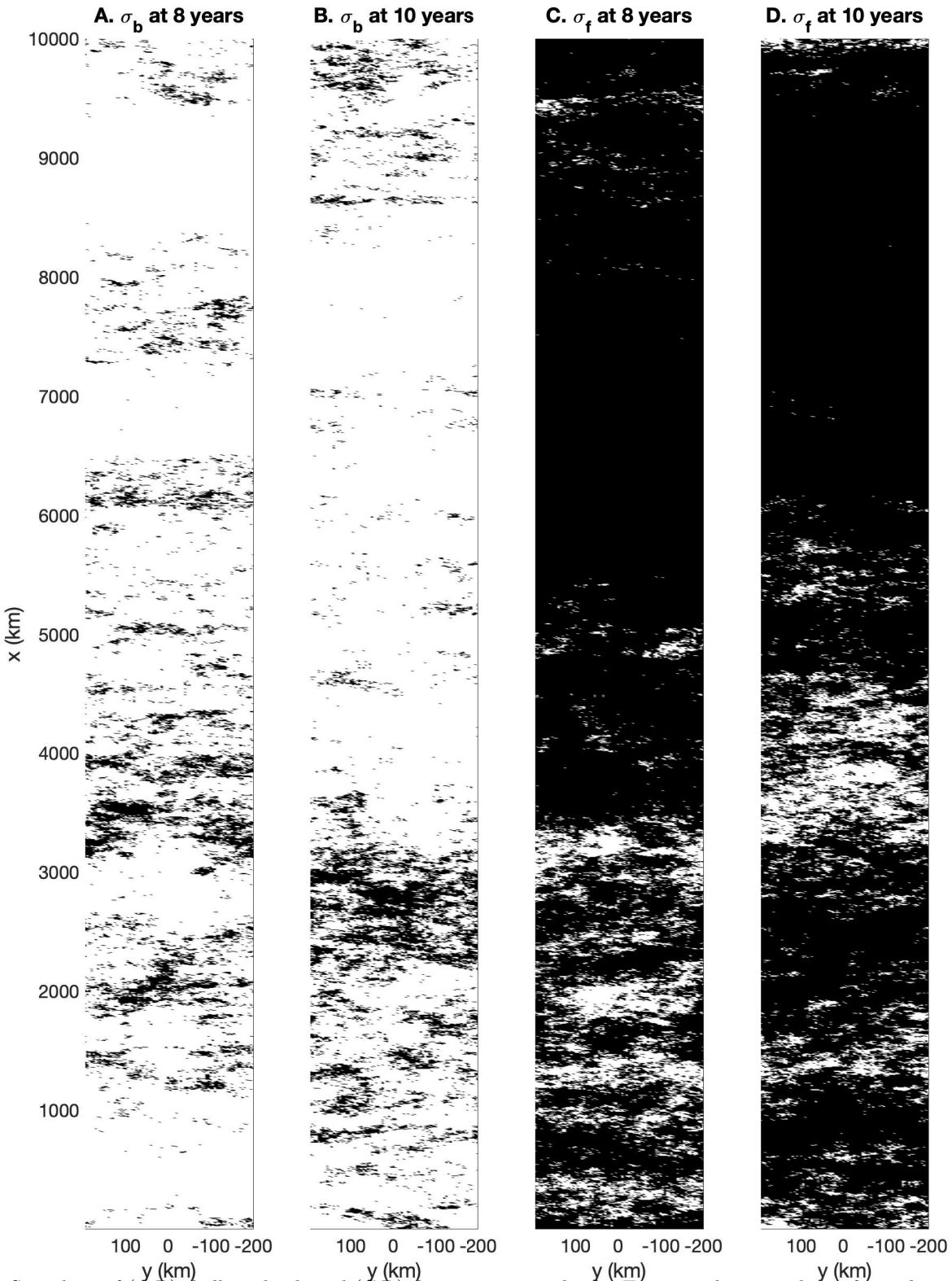

FIG. 8. Snapshots of (A,B) shallow clouds and (C,D) deep convective clouds. Two snapshots are shown for each quantity, one at the time of 8 years and one at the time of 10 years. White color indicates the presence of cloud, and black color indicates the absence of cloud. The domain has been rotated counterclockwise by 90° to fit on the page, and the western warm pool region appears in the bottom and the eastern cold pool region appears on the top.

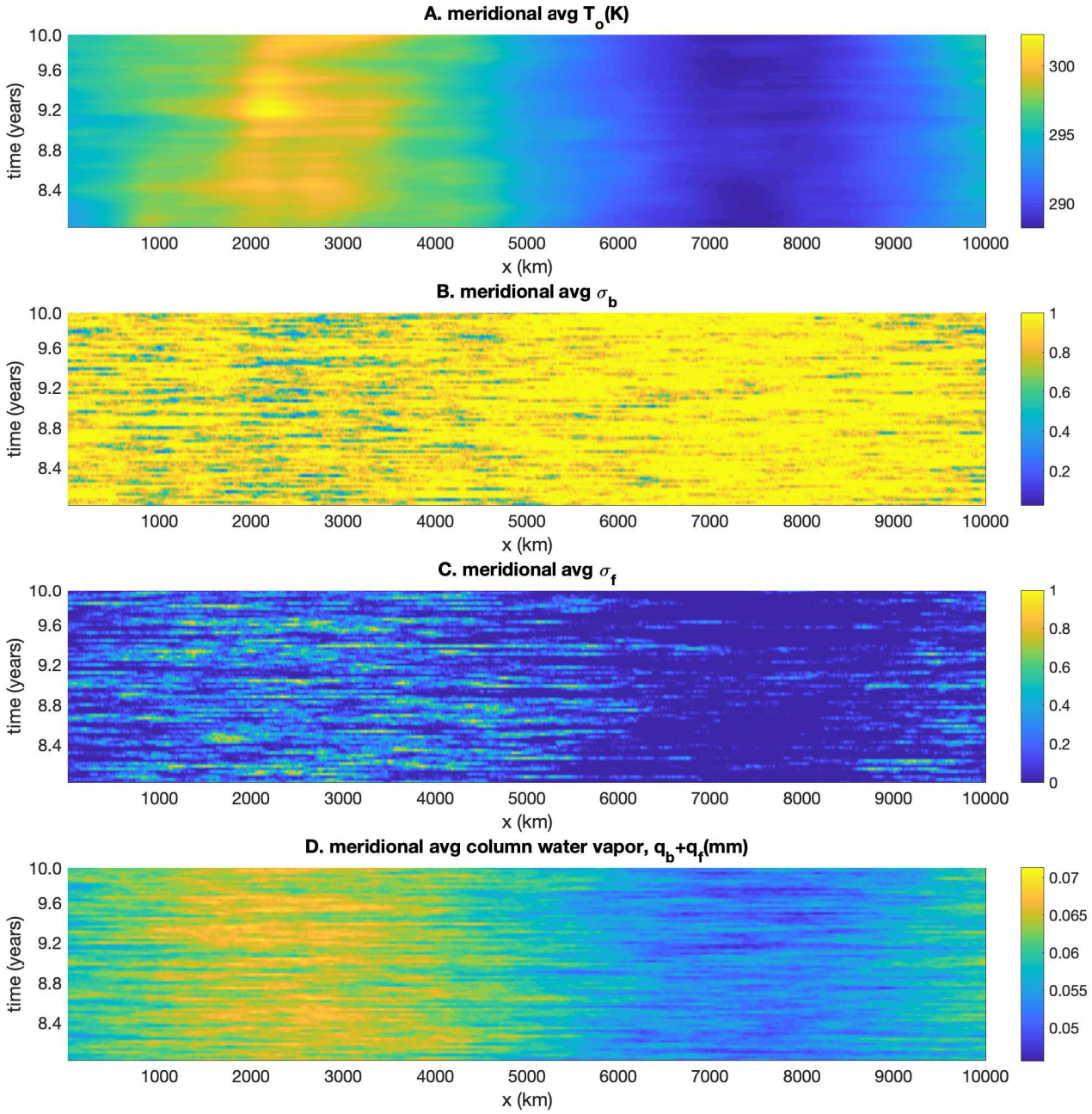

FIG. 9. Space-and-time evolution plot of model variables (meridionally-averaged) from the simulation with standard parameters during the last two years: (A) Ocean temperature. (B) Shallow cloud fraction. (C) Deep convective cloud fraction. (D) Total column water vapor.

that deep convection is more common. Furthermore, the region of deep convection has expanded significantly in its area; in the climate-change simulation in Fig. 10C, the region where time-averaged $\sigma_f > 0.3$ is roughly 40% of the domain, in comparison to roughly 10 to 20% of the domain in the standard simulation in Fig. 7C. While the deep convective patterns change, the circulation did not show any substantial change between the standard and

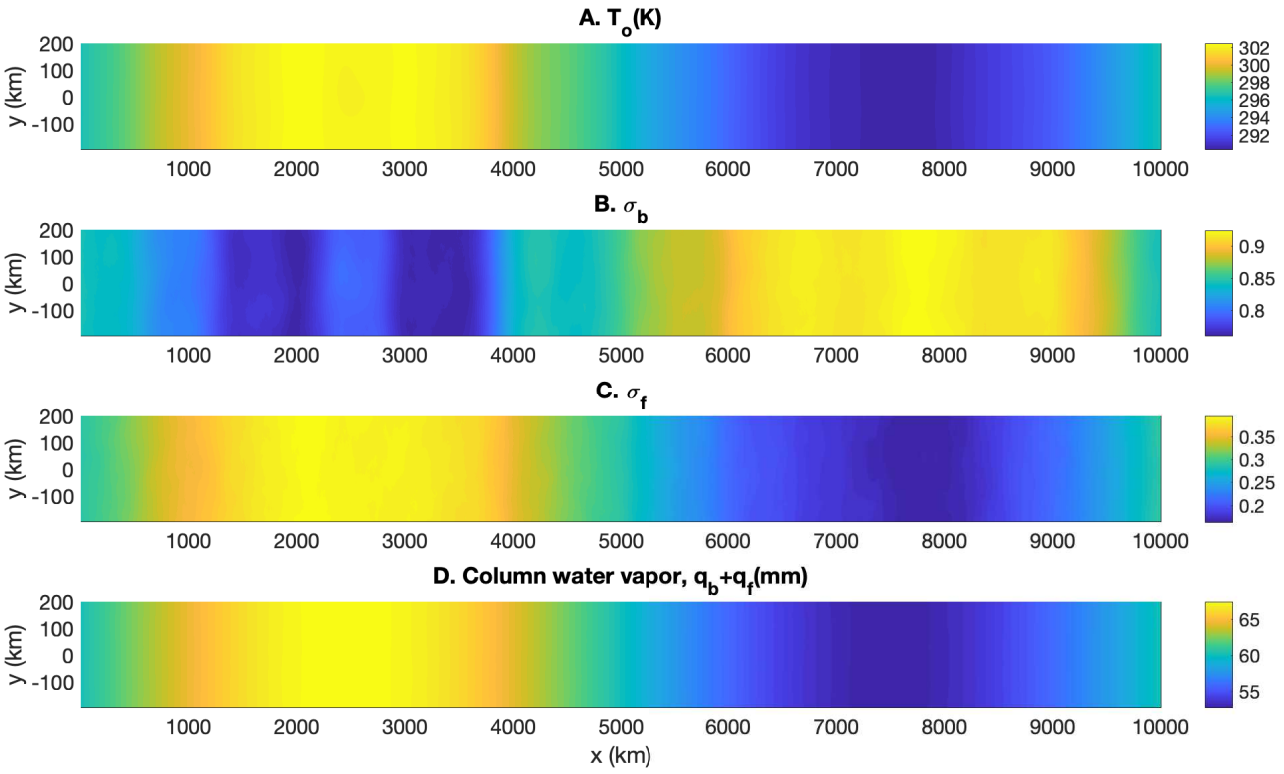

FIG. 10. The mean climate state (i.e., time-averaged quantities), as in Fig. 7, except from the climate-change simulation with enhanced longwave absorptivity parameters $a^0_{lb} = 0.288$ and $a^0_{lf} = 0.48$. The climate state here has an expanded warm pool region in the western part of the domain, associated with more deep convection (panel C) and more moisture (panel D) in comparison to the standard simulation in Fig. 7.

climate-change scenarios, which is consistent with the mixture of evidence from nature of small or inconclusive changes [13, 66, 67]. Another interesting change is that deep convection is now forming everywhere in the domain in the climate-change simulation, since the time-averaged σ_f is greater than 0.1 essentially everywhere in Fig. 10C, whereas a region of essentially zero deep convection could be seen within the cold pool region in Fig. 7C in the standard simulation.

Meridional averages—i.e., averages over the y coordinate—are shown in Fig. 11 for comparison of the mean climate states of both the standard parameter simulation and climate-change simulation. In Fig. 11A and D, one can see that the ocean is warmer and the atmosphere is more moist in the climate-change scenario. Also, the enhancement of deep convection over both the warm pool and cold pool is shown in Fig. 11B, while the shallow cloud fraction decreased globally at the same time. In the climate-change scenario, the shallow cloud fraction decreased, which decreases the cooling effect of shallow clouds (by allowing more solar radiation to reach the boundary layer), and is consistent with a warming of the boundary layer and ocean temperature.

As another comparison, Fig. 12 shows time series of domain-averaged quantities from both the standard simulation and the climate-change simulation. The domain-averaged quantities shown are (A) ocean temperature, (B) boundary-layer temperature, (C) free-tropospheric temperature, (D) shallow cloud fraction, and (E) deep convective cloud fraction. The most substantial difference between the two simulations is a large global warming in the ocean and boundary layer temperatures. The free-tropospheric temperature is slightly colder in the climate-change simulation, although the difference is small; it could be due to the simplistic treatment here of radiation and in particular cloud feedbacks and would be interesting to investigate further in the future. Deep convection is more active, as also mentioned above, and the shallow cloud fraction, on the other hand, has decreased. Hence the model simulations show some of the basic feedbacks involved in climate change. In addition, the model framework includes substantial fluctuations in time, and the system is not in a fixed equilibrium state but in a statistical equilbrium.

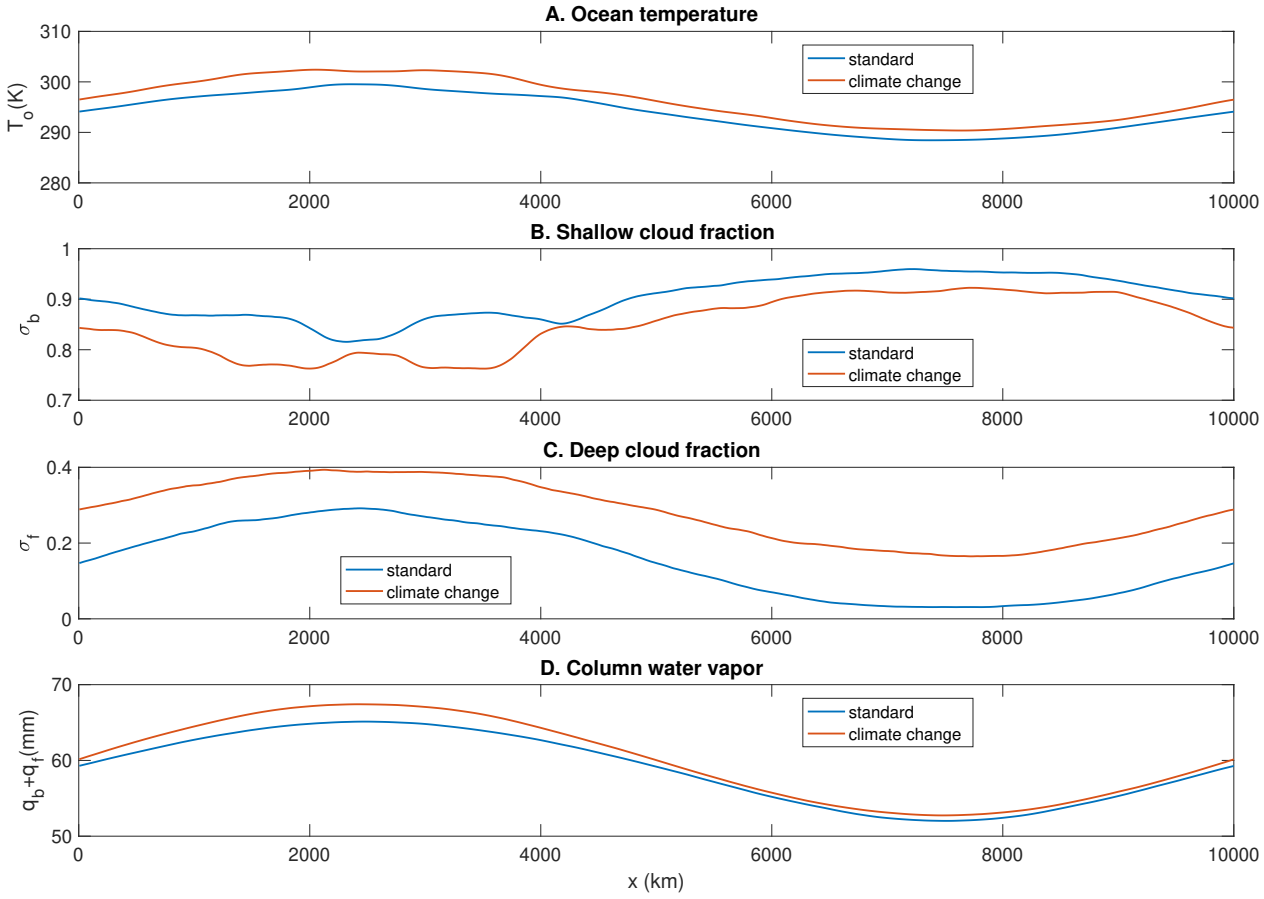

FIG. 11. Mean climate states in the standard simulation versus climate-change scenario, presented as functions of the zonal coordinate x after a time-average and meridional-average. (A) ocean temperature, (B) shallow cloud fraction, (C) deep cloud fraciton, (D) column water vapor.

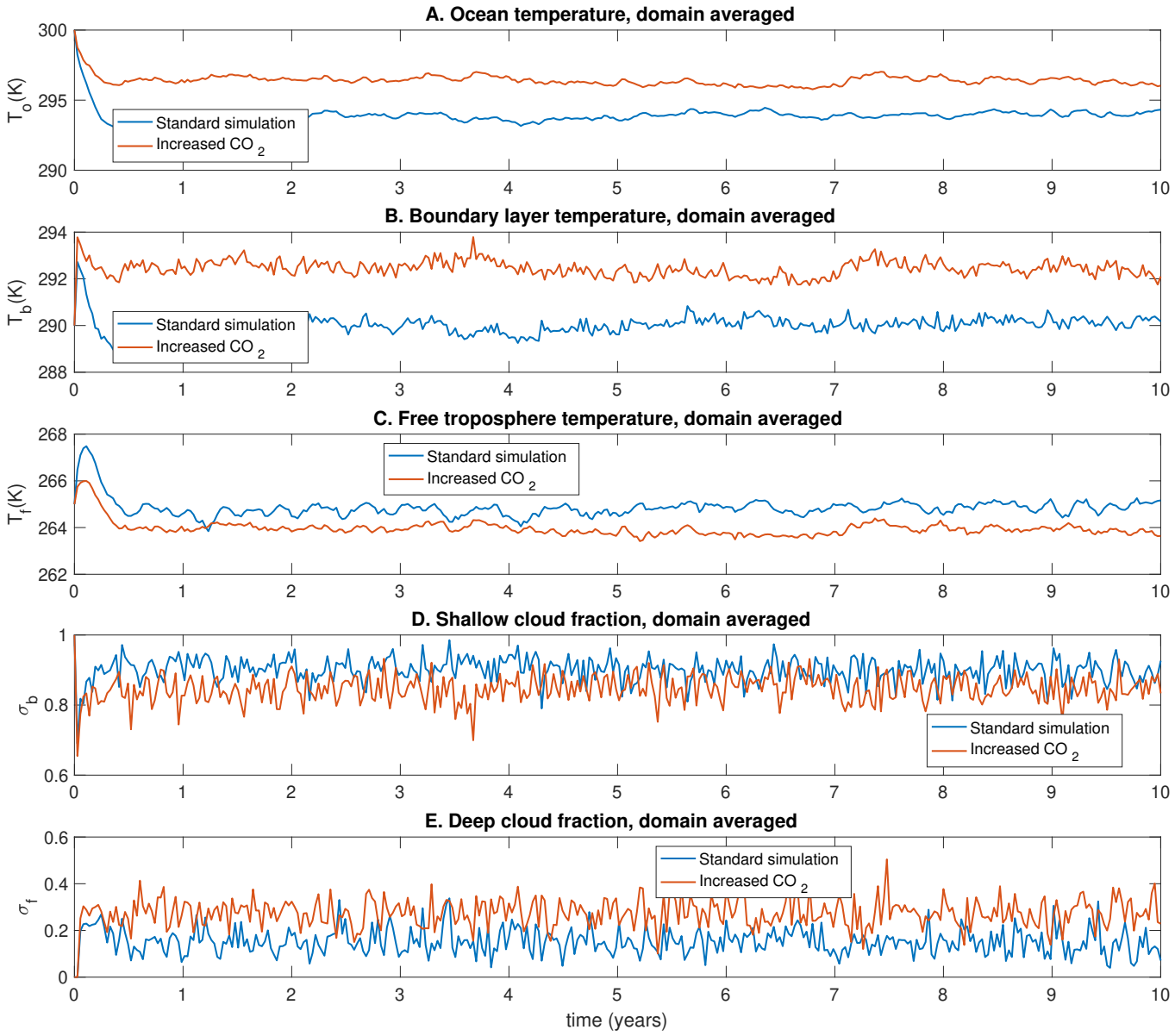

FIG. 12. Time series of domain-averaged quantities, and comparison between the standard simulation and the climate-change simulation: (A) ocean temperature, (B) boundary layer temperature, (C) free-tropospheric temperature, (D) shallow cloud fraction, (E) deep convective cloud fraction.

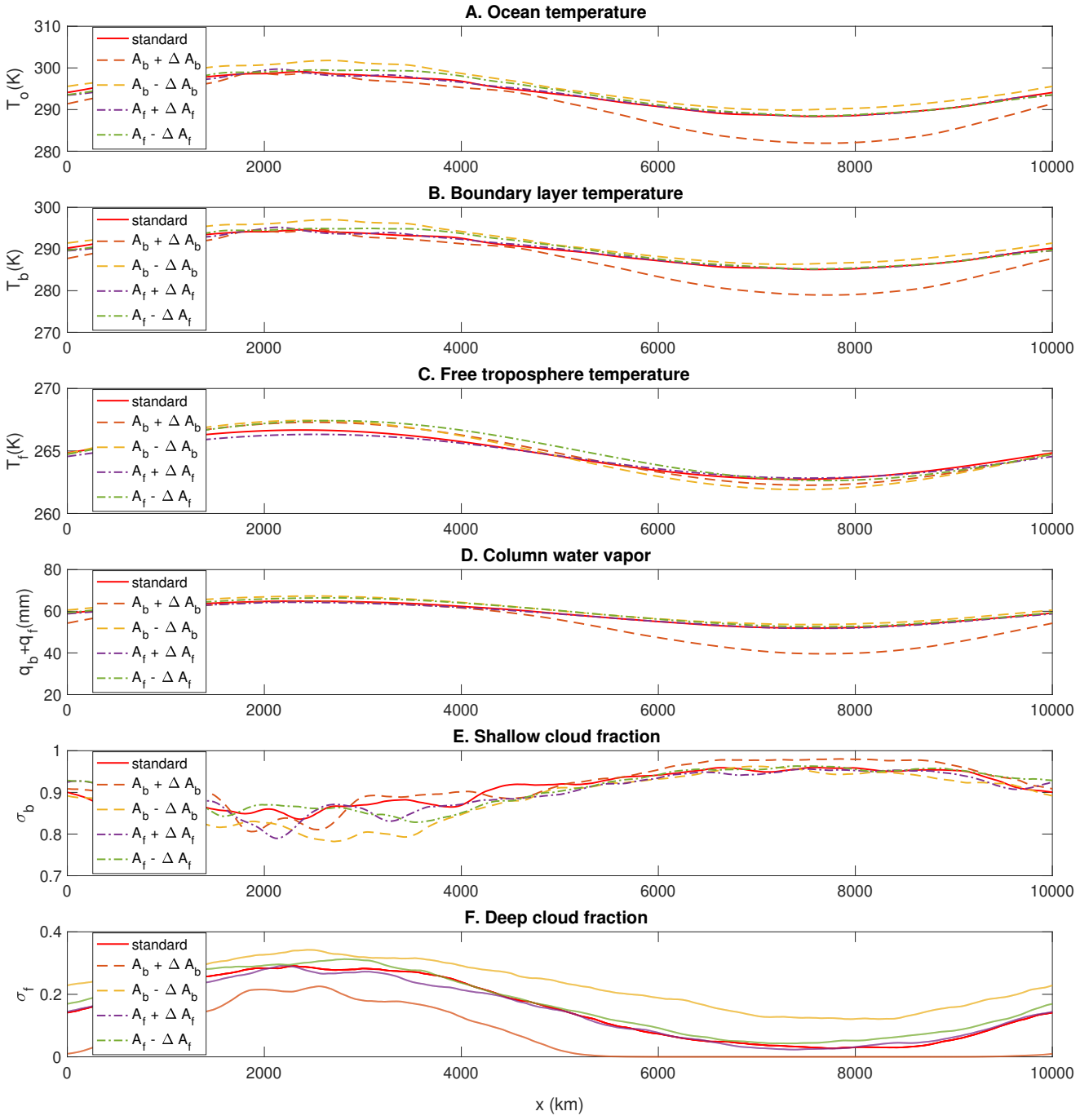

FIG. 13. Sensitive study involving the two cloud albedo parameters A_b and A_f. Statistics of model variables are time-averaged and meridionally-averaged. Solid lines show the simulation result with standard parameters, dashed lines show results under modification $\pm\Delta A_b$ of the shallow cloud albedo, and dash–dot lines show results under modification $\pm\Delta A_f$ of the deep convective cloud albedo. The adjustment values are $\Delta A_b = \Delta A_f = 0.05$.

Finally, we explore parameter space and assess the sensitivity to the two cloud albedos, A_b and A_f. To do so,

we run several simulations under the standard parameters, except with modified values of the shallow cloud albedo $A_b \pm \Delta A_b$ and deep convective albedo $A_f \pm \Delta A_f$, with adjustment values of ΔA_b and ΔA_f both equal to 0.05. For each single simulation experiment, we only modified one of these parameters. All simulations were run for 3 years with the first year to reach an approximate statistical equilibrium and the last 2 years to collect time-averaged data. The time-averaged data were further meridionally-averaged and are shown in Fig. 13. The first three panels show the influence on temperatures, panel D shows the change of moisture, while the last two panels E and F present changes in the cloud fractions. From this plot, one can see that the broad features are essentially the same in the standard case and the sensitivity studies, in terms of the positive versus negative anomalies in the western versus eastern sides of the domain (or vice versa). One can also see some differences arising, such as a greater sensitivity to shallow cloud albedo perturbation ΔA_b rather than deep cloud albedo perturbation ΔA_f, and a greater sensitivity to the positive perturbation $+\Delta A_b$ than the negative perturbation $-\Delta A_b$ in the eastern half of the domain. The greater sensitivity to shallow cloud albedo is reminiscent of studies that have identified the key role of shallow clouds in climate sensitivity and uncertainties in climate models [6, 7].

IV. CONCLUDING DISCUSSION

A modeling framework was investigated here for the possibility of idealized climate simulations with individual clouds and stratocumulus clouds on planetary-scale domains. To achieve computational efficiency, the clouds are modeled stochastically, and simplified vertical structures are assumed to reduce the number of gridded spatial dimensions from three to two. The basic structure of the model is a combination of a large-scale fluid dynamics model that resolves weather/climate variability but not individual cloud circulations, and spatiotemporal stochastic models for smaller-scale turbulent advection–diffusion of water vapor and clouds.

Numerical simulations were presented to test whether an idealized climate state can be generated with evolving and interactive clouds. The basic regional differences were seen in different cloud types, including a warm pool region with a higher level of deep convection and a cold pool region with a lower level of deep convection and an expansive stratocumulus cloud deck. Individual clouds can form and decay and have different lifetimes and sizes, and the climate state is not a fixed equilibrium state but a dynamic evolution in a statistical equilibrium.

It would be interesting in the future to consider additional processes in the model, to potentially bring in an even higher level of realism. For example, upper tropospheric clouds such as stratiform or cirrus or anvil clouds have their own distinctive radiative effects which can influence the climate, and they were not included here but could be added in the future. In the boundary layer as well as the free troposphere, nonlinear advection of moisture was not included here but could be added for further realism. Also, by including a more complex treatment of deep convection or ocean dynamics, it may be possible to include additional aspects of climate variability such as convectively coupled equatorial waves (CCEWs), the Madden–Julian oscillation (MJO), and the El Niño–Southern Oscillation (ENSO).

A benefit of simplified models is that it is relatively easy for different physical processes to be included, excluded, or modified, and the impact can be measured. In the present paper, several sensitivities were explored, including changes to cloud albedo and their impact on cloud–radiative feedbacks. In the different sensitivity studies here, the climate-scale circulations showed minimal sensitivity, and it would be interesting in the future to explore their sensitivity to other processes. For instance, in addition to the other processes mentioned in the previous paragraph, it would also be interesting to consider different formulations of the stochastic clouds, such as stochastic entrainment or additional cloud types.

Given that the simulations displayed some of the basic features of climate-change scenarios, it would also be interesting in the future to investigate questions about individual clouds, their statistics, and global warming. For example, in this model framework, it is not only bulk averaged cloud properties (such as area fractions) that are available, but also individual cloud properties such as lifetimes and areas. It is then possible to examine cloud–radiative feedback processes related to these individual cloud properties. As another example, extreme events can be quantified in this model framework in terms of cloud cluster areas or rain event sizes. It would be interesting to investigate changes in extreme events in this model under different global warming scenarios.

ACKNOWLEDGMENTS

The authors thank two anonymous reviewers for helpful comments. The research of S.N.S. and T.H. was partially supported by a Vilas Associates Award from the University of Wisconsin-Madison Office of the Vice Chancellor for Research and Graduate Education with funding from the Wisconsin Alumni Research Foundation. J.L.T. is supported by a Department of Energy Computational Science Graduate Fellowship under grant DE-SC0020347.

[1] G. W. Petty, *A first course in atmospheric radiation* (Sundog Pub, Madison, Wisconsin, USA, 2006).
[2] J. D. Neelin, *Climate change and climate modeling* (Cambridge University Press, New York, 2010).
[3] IPCC, *Climate Change 2013: The Physical Science Basis. Working Group I Contribution to the Fifth Assessment Report of the Intergovernmental Panel on Climate Change*, edited by T. Stocker, D. Qin, M. Plattner, G.-K. Tignor, S. Allen, J. Boschung, A. Nauels, Y. Xia, B. Bex, and P. Midgley (Cambridge University Press, New York, 2013).
[4] R. D. Cess, G. L. Potter, J. P. Blanchet, G. J. Boer, A. D. Del Genio, M. Deque, V. Dymnikov, V. Galin, W. L. Gates, S. J. Ghan, *et al.*, Intercomparison and interpretation of climate feedback processes in 19 atmospheric general circulation models, J. Geophys. Res. **95**, 16601 (1990).
[5] G. L. Stephens, Cloud feedbacks in the climate system: A critical review, J. Climate **18**, 237 (2005).
[6] S. Bonyand J. Dufresne, Marine boundary layer clouds at the heart of tropical cloud feedback uncertainties in climate models, Geophys. Res. Lett **32**, 20806 (2005).
[7] S. Bony, B. Stevens, D. M. Frierson, C. Jakob, M. Kageyama, R. Pincus, T. G. Shepherd, S. C. Sherwood, A. P. Siebesma, A. H. Sobel, *et al.*, Clouds, circulation and climate sensitivity, Nature Geoscience **8**, 261 (2015).

[8] B. Stevens, Atmospheric moist convection, Annu. Rev. Earth Planet. Sci. **33**, 605 (2005).

[9] B. Stevens, C.-H. Moeng, A. S. Ackerman, C. S. Bretherton, A. Chlond, S. de Roode, J. Edwards, J.-C. Golaz, H. Jiang, M. Khairoutdinov, *et al.*, Evaluation of large-eddy simulations via observations of nocturnal marine stratocumulus, Mon. Wea. Rev. **133**, 1443 (2005).

[10] S. N. Stechmann, Multiscale eddy simulation for moist atmospheric convection: Preliminary investigation, J. Comput. Phys. **271**, 99 (2014).

[11] G. Matheou, D. Chung, and J. Teixeira, Large-eddy simulation of a stratocumulus cloud, Physical Review Fluids **2**, 090509 (2017).

[12] J. P. Mellado, Cloud-top entrainment in stratocumulus clouds, Annual Review of Fluid Mechanics **49**, 145 (2017).

[13] S. N. Stechmannand H. R. Ogrosky, The Walker circulation, diabatic heating, and outgoing longwave radiation, Geophys. Res. Lett. **41**, 9097 (2014).

[14] E.-S. Chung, A. Timmermann, B. J. Soden, K.-J. Ha, L. Shi, and V. O. John, Reconciling opposing walker circulation trends in observations and model projections, Nature Climate Change **9**, 405 (2019).

[15] C. J. Muller, P. A. OGorman, and L. E. Back, Intensification of precipitation extremes with warming in a cloud-resolving model, Journal of Climate **24**, 2784 (2011).

[16] D. M. Romps, Response of tropical precipitation to global warming, Journal of the Atmospheric Sciences **68**, 123 (2011).

[17] M. Khairoutdinovand C.-E. Yang, Cloud-resolving modelling of aerosol indirect effects in idealised radiative-convective equilibrium with interactive and fixed sea surface temperature, Atmospheric Chemistry and Physics **13**, 4133 (2013).

[18] C. Mullerand Y. Takayabu, Response of precipitation extremes to warming: what have we learned from theory and idealized cloud-resolving simulations, and what remains to be learned?, Environmental Research Letters **15**, 035001 (2020).

[19] C. S. Bretherton, Challenges in numerical modeling of tropical circulations, in *The Global Circulation of the Atmosphere*, edited by T. Schneiderand A. H. Sobel (Princeton University Press, Princeton, 2007) Chap. 11, pp. 302–330.

[20] W. W. Grabowskiand P. K. Smolarkiewicz, CRCP: a Cloud Resolving Convection Parameterization for modeling the tropical convecting atmosphere, Physica D: Nonlinear Phenomena **133**, 171 (1999).

[21] S. Hottovyand S. N. Stechmann, A spatiotemporal stochastic model for tropical precipitation and water vapor dynamics, J. Atmos. Sci. **72**, 4721 (2015).

[22] S. N. Stechmannand S. Hottovy, Cloud regimes as phase transitions, Geophys. Res. Lett. **43**, 6579 (2016).

[23] F. Ahmedand J. D. Neelin, Explaining scales and statistics of tropical precipitation clusters with a stochastic model, Journal of the Atmospheric Sciences **76**, 3063 (2019).

[24] B. Khouiderand A. Bihlo, A new stochastic model for the boundary layer clouds and stratocumulus phase transition regimes: Open cells, closed cells, and convective rolls, Journal of Geophysical Research: Atmospheres **124**, 367 (2019).

[25] D. L. Monroyand G. G. Naumis, Description of mesoscale pattern formation in shallow convective cloud fields by using time-dependent ginzburg-landau and swift-hohenberg stochastic equations, Physical Review E **103**, 032312 (2021).

[26] J. D. Neelinand N. Zeng, A quasi-equilibrium tropical circulation model—formulation, J. Atmos. Sci. **57**, 1741 (2000).

[27] J. Linand J. Neelin, Influence of a stochastic moist convective parameterization on tropical climate variability, Geophys. Res. Lett. **27**, 3691 (2000).

[28] B. Khouiderand A. J. Majda, A non-oscillatory balanced scheme for an idealized tropical climate model: Part I: Algorithm and validation, Theor. Comp. Fluid Dyn. **19**, 331 (2005).

[29] B. Khouiderand A. J. Majda, Multicloud convective parameterizations with crude vertical structure, Theor. Comp. Fluid Dyn. **20**, 351 (2006).

[30] B. Khouider, J. A. Biello, and A. J. Majda, A stochastic multicloud model for tropical convection, Comm. Math. Sci. **8**, 187 (2010).

[31] Y. Frenkel, A. J. Majda, and S. N. Stechmann, Cloud-radiation feedback and atmosphere-ocean coupling in a stochastic multicloud model, Dyn. Atmos. Oceans **71**, 35 (2015).

[32] Y. Chenand S. N. Stechmann, Multi-model communication and data assimilation for mitigating model error and improving forecasts, Chin. Ann. Math. Ser. B **40**, 689 (2019).

[33] A. J. Majda, *Introduction to PDEs and Waves for the Atmosphere and Ocean*, Courant Lecture Notes in Mathematics, Vol. 9 (American Mathematical Society, Providence, 2003) pp. x+234.

[34] S. N. Stechmann, A. J. Majda, and B. Khouider, Nonlinear dynamics of hydrostatic internal gravity waves, Theor. Comp. Fluid Dyn. **22**, 407 (2008).

[35] M. A. Kellyand D. A. Randall, A two-box model of a zonal atmospheric circulation in the tropics, J. Climate **14**, 3944 (2001).

[36] E. A. Muellerand S. N. Stechmann, Shallow-cloud impact on climate and uncertainty: A simple stochastic model, Mathematics of Climate and Weather Forecasting **6**, 16 (2020).

[37] R. Marchandand T. Ackerman, A cloud-resolving model with an adaptive vertical grid for boundary layer clouds, Journal of the atmospheric sciences **68**, 1058 (2011).

[38] W. W. Grabowski, Towards global large eddy simulation: Super-parameterization revisited, Journal of the Meteorological Society of Japan. Ser. II **94**, 327 (2016).

[39] H. Parishani, M. S. Pritchard, C. S. Bretherton, M. C. Wyant, and M. Khairoutdinov, Toward low-cloud-permitting cloud superparameterization with explicit boundary layer turbulence, Journal of Advances in Modeling Earth Systems **9**, 1542 (2017).

[40] D. H. Marsicoand S. N. Stechmann, Expanding grids for efficient cloud dynamics simulations across scales, Mathematics of Climate and Weather Forecasting **6**, 38 (2020).

[41] M. L. Waiteand B. Khouider, Boundary layer dynamics in a simple model for convectively coupled gravity waves, J. Atmos.

Sci. **66**, 2780 (2009).
[42] J. A. Bielloand A. J. Majda, Boundary layer dissipation and the nonlinear interaction of equatorial baroclinic and barotropic Rossby waves, Geophys. Astrophys. Fluid Dynam. **98**, 85 (2004).
[43] R. Neggers, B. Stevens, and J. Neelin, A simple equilibrium model for shallow-cumulus-topped mixed layers, Theoretical and Computational Fluid Dynamics **20**, 305 (2006).
[44] A. H. Sobeland J. D. Neelin, The boundary layer contribution to intertropical convergence zones in the quasi-equilibrium tropical circulation model framework, Theoretical and Computational Fluid Dynamics **20**, 323 (2006).
[45] B. Stevens, Bulk boundary-layer concepts for simplified models of tropical dynamics, Theor. Comp. Fluid Dyn. **20**, 279 (2006).
[46] S. N. Stechmannand S. Hottovy, Unified spectrum of tropical rainfall and waves in a simple stochastic model, Geophys. Res. Lett. **44**, 10,713 (2017).
[47] N. A. Phillips, Energy transformations and meridional circulations associated with simple baroclinic waves in a two-level, quasi-geostrophic model, Tellus **6**, 273 (1954).
[48] N. A. Phillips, The general circulation of the atmosphere: A numerical experiment, Quarterly Journal of the Royal Meteorological Society **82**, 123 (1956).
[49] I. M. Held, The gap between simulation and understanding in climate modeling, Bulletin of the American Meteorological Society **86**, 1609 (2005).
[50] G. Vallis, *Atmospheric and Oceanic Fluid Dynamics: Fundamentals and Large-scale Circulation* (Cambridge University Press, New York, 2006).
[51] R. Hu, T. K. Edwards, L. M. Smith, and S. N. Stechmann, Initial investigations of precipitating quasi-geostrophic turbulence with phase changes, Research in the Mathematical Sciences **8**, https://doi.org/10.1007/s40687-020-00242-3 (2021).
[52] B. E. Mapesand R. A. Houze Jr., Diabatic divergence profiles in western Pacific mesoscale convective systems, J. Atmos. Sci. **52**, 1807 (1995).
[53] G. N. Kiladis, M. C. Wheeler, P. T. Haertel, K. H. Straub, and P. E. Roundy, Convectively coupled equatorial waves, Rev. Geophys. **47**, RG2003 (2009).
[54] R. Rogersand M. Yau, *A short course in cloud physics* (Butterworth–Heinemann, Burlington, 1989).
[55] J. D. Neelin, O. Peters, and K. Hales, The transition to strong convection, J. Atmos. Sci. **66**, 2367 (2009).
[56] R. Salmon, *Lectures on Geophysical Fluid Dynamics* (Oxford University Press, New York, 1998).
[57] A. J. Majdaand P. R. Kramer, Simplified models for turbulent diffusion: theory, numerical modelling, and physical phenomena, Phys. Rep. **314**, 237 (1999).
[58] T. DelSole, Stochastic models of quasigeostrophic turbulence, Surv. Geophys. **25**, 107 (2004).
[59] A. J. Majdaand M. J. Grote, Explicit off-line criteria for stable accurate time filtering of strongly unstable spatially extended systems, Proc. Natl. Acad. Sci. USA **104**, 1124 (2007).
[60] A. J. Majdaand M. J. Grote, Mathematical test models for superparametrization in anisotropic turbulence, Proc. Natl. Acad. Sci. USA **106**, 5470 (2009).
[61] W. W. Grabowskiand P. K. Smolarkiewicz, Two-time-level semi-Lagrangian modeling of precipitating clouds, Mon. Wea. Rev. **124**, 487 (1996).
[62] M. E. Petersand C. S. Bretherton, A simplified model of the Walker circulation with an interactive ocean mixed layer and cloud–radiative feedbacks, J. Climate **18**, 4216 (2005).
[63] C. W. Gardiner, *Handbook of stochastic methods: for physics, chemistry & the natural sciences*, Springer Series in Synergetics, Vol. 13 (Springer–Verlag, Berlin, 2004).
[64] J. L. Torchinskyand S. N. Stechmann, EZ Parallel version 1.0, Github Repository (2020).
[65] O. Peters, J. D. Neelin, and S. W. Nesbitt, Mesoscale convective systems and critical clusters, J. Atmos. Sci. **66**, 2913 (2009).
[66] G. A. Vecchi, B. J. Soden, A. T. Wittenberg, I. M. Held, A. Leetmaa, and M. J. Harrison, Weakening of tropical Pacific atmospheric circulation due to anthropogenic forcing, Nature **441**, 73 (2006).
[67] M. L. L'Heureux, S. Lee, and B. Lyon, Recent multidecadal strengthening of the Walker circulation across the tropical Pacific, Nature Climate Change **3**, 571 (2013).